Spaceborne GNSS-R Bistatic Radar Remote Sensing, CYGNSS, and Future Missions

By Christopher Ruf, *Life Fellow IEEE*, and Scott Gleason, *Senior Member IEEE*

ABSTRACT | Global Navigation Satellite System Reflectometry (GNSS-R) is a relatively new type of radar developed for remote sensing of the Earth surface. It uses GNSS navigation signals such as those transmitted by the Global Positioning System (GPS) constellation of satellites as the radar transmitter. The radar receiver measures alterations in the navigation signal caused by scattering from the Earth surface. The nature of those alterations contains information about the surface, which can be retrieved. The general theory of GNSS-R remote sensing and its historical development is presented, followed by a detailed assessment of the performance and capabilities of the first dedicated spaceborne GNSS-R science mission, NASA's Cyclone Global Navigation Satellite System (CYGNSS). Numerous follow-on GNSS-R missions are also noted that have either already been launched or are scheduled to be soon. A wide range of science data products and scientific applications of the CYGNSS data are examined. Developments that are currently underway in GNSS-R technology are summarized, and their potential impact on the capabilities of future GNSS-R missions is discussed.

KEYWORDS | Bistatic radar; Cyclone Global Navigation Satellite System (CYGNSS); Global Navigation Satellite System Reflectometry (GNSS-R).

Received 5 March 2025; revised 29 May 2025 and 25 June 2025; accepted 25 June 2025. This work was supported in part by the National Aeronautics and Space Administration (NASA) Science Mission Directorate Contract with the University of Michigan under Grant 80LARC21DA003. *(Corresponding author: Christopher Ruf.)*

Christopher Ruf is with the Department of Climate and Space Sciences and Engineering, University of Michigan, Ann Arbor, MI 48109 USA (e-mail: cruf@umich.edu).

Scott Gleason is with Daaxa LLC, Boulder, CO 80305 USA (e-mail: sgleason@protonmail.com).

Digital Object Identifier 10.1109/JPROC.2025.3583997

I. Introduction

The history of Global Navigation Satellite System Reflectometry (GNSS-R) had a pessimistic start. In 1988, Hall and Cordey [1] floated the idea of using Global Positioning System (GPS) transmitters in a multistatic configuration for sensing the ocean surface, but concluded that the concept was "inadequate" because "transmitters of much higher power are required to realize a system with useful performance." This assessment turned out to be spectacularly mistaken. It turns out that GNSS signals reflecting off the Earth's surface are not only detectable from near Earth platforms (aircraft, balloons, etc.) but also from low Earth orbiting (LEO) satellites. The two main applications of these reflections were proposed several years later, first for ocean surface altimetry in 1993 [2], followed by using the signals as a bistatic scatterometer in 1998 [3].

These results were followed in rapid succession by a series of experimental validations of GNSS-R to retrieve ocean surface winds with instruments carried on a variety of platforms, including aircraft [4], [5], [6] and a high-altitude balloon [7] in the early 2000s. In parallel, a detailed theoretical model was developed to provide a foundational understanding of the underlying scattering mechanisms. This theoretical basis for the geophysical parameter retrievals that followed was published by Zavorotny and Voronovich [8]. It combined a model for the ocean surface roughness spectrum developed by Elfouhaily et al. [9] with the unique characteristics of an *L*-band GNSS signal and described the signal processing requirements of the GNSS-R radar receiver.

A. Early Spaceborne Observations

At about the same time, in 2002, a tantalizing possibility was demonstrated with the first detection (including

© 2025 The Authors. This work is licensed under a Creative Commons Attribution 4.0 License.
For more information, see https://creativecommons.org/licenses/by/4.0/

delay power mapping) of a nadir-oriented reflected GNSS signal from LEO, due to a fortuitous data grab from an instrument on the International Space Station (ISS) [10]. At roughly the same time, Earth surface reflections were detected in radio holograms retrieved from the raw data of the GNSS radio occultation instruments at grazing angle geometries on the GPS/MET [113] and CHAMP [114] missions in 2001 and 2002, respectively. The ISS result was achieved using a very high-gain antenna, and it was still uncertain if reflected signals could be detected using more manageable instrument configurations on small satellites. That question was answered affirmatively using another "bit-grabber" experiment added to the U.K.-Disaster Monitoring Constellation (UK-DMC) satellite in 2003 [11]. This experiment consisted of an ∼11.8-dB gain left-hand circular polarized (LHCP) downward looking antenna (the opposite polarization of the transmitted GNSS signals, to account for the general polarization flip on reflection), and a small daughter board added between the GPS navigation receiver and a spare data recorder located in the same spacecraft tray. Using a commanded data-grab mode, it was possible to capture and downlink targeted surface collections during the mission lifetime (on the order of a couple hundred collections, each of ∼20-s duration, over the course of the mission). These results showed conclusively that GNSS-reflected signals were detectable and could be linked to surface characteristics for ocean [12], as well as land and sea ice [13], [14]. For the ocean demonstration, UK-DMC data collections were targeted near ocean buoys, providing a limited but sufficient dataset to show the signal changes in spread and magnitude with respect to varying ocean wind speed conditions allowed for a simple ocean sensing geophysical model function (GMF) to be generated, and ocean wind estimates to be made [15].

By this point, the flood gates had been breached and multiple demonstrations of GNSS-R applications were appearing in rapid succession, including the sensing of land-surface soil moisture [16], [17] and Arctic sea ice [18] from aircraft platforms. Additionally, the feasibility of spaceborne GNSS-R altimetry using coherently reflected carrier phase was demonstrated using the CHAMP GNSS-RO instrument in 2004 [115]. With the stage set, the next significant step in the maturation of GNSS-R was only a matter of time: a dedicated spacecraft remote sensing mission. This breakthrough occurred in 2012 with the selection of the NASA Cyclone Global Navigation Satellite System (CYGNSS) Mission [19] and the associated precursor Technology Demonstration Satellite (TDS) developed by the U.K. Space Agency, European Space Agency (ESA), and Surrey Satellite Technology Ltd. (SSTL). Both TDS and CYGNSS carried the same GNSS-R instrument, capable of generating real-time observations of surface reflections. Previously, with UK-DMC, all of the surface reflections were postprocessed on the ground using relatively short raw data captures. The instrument on CYGNSS and TDS contained a real-time observation tracker and delay–Doppler map (DDM) processor, capable of generating four parallel reflection observations at 100% duty cycle, thus increasing the volume of DDM science observations available to the community by several orders of magnitude [20], [21].

The single TDS satellite was launched on July 8, 2014, into a near-circular 635-km sun-synchronous orbit at 98.8° inclination. It carried eight separate payloads, which were under development by SSTL, with the objective of demonstrating and characterizing their performance on orbit. One of these payloads was the SSTL GNSS Receiver-Remote Sensing Instrument (SGR-ReSI) [22]. Because TDS was oversubscribed with payloads relative to the power and data-handling capacities of the satellite bus, the SGR-ReSI could only be operated ∼25% of the time. This duty cycle was more than sufficient to demonstrate its engineering functionality and scientific potential. Early scientific applications of the DDM observations made by TDS before its end of life on May 31, 2019, included the retrieval of near-surface winds over the ocean [23] and of subsurface soil moisture over land [24]. These and other scientific applications soon carried over to the CYGNSS Mission. Additional summaries of the history and fundamental concepts of GNSS-R and its science applications can be found in [25] and [26]. Although not covered in detail here, there has also been extensive use of ground-based GNSS-R instruments used in networks to monitor, tides, soil moisture [116], and snow [117]. An overview of GNSS-R ground observations can be found in [118].

B. NASA CYGNSS Earth Venture Mission

CYGNSS consists of eight satellites carrying SGR-ReSI payloads, denoted on CYGNSS as the delay–Doppler mapping instrument (DDMI). Notably, whereas the SGR-ReSI on TDS was connected to a single GPS receive antenna pointed close to the nadir direction, each DDMI on CYGNSS was connected to a pair of antennas pointed in the port and starboard azimuthal direction at an off-nadir angle of ∼28°. This configuration significantly increases the field of view on the surface within which a GPS specular reflection point must lie in order to be measured. This, in turn, increases the number of reflections available and the spatial sampling coverage that results. The use of multiple satellites further increases the spatial sampling coverage. The CYGNSS constellation was launched on December 15, 2016, into a near-circular 520-km orbit at 35° inclination. The orbit was chosen to maximize time spent over latitudes with the highest probability of occurrence of tropical cyclones, which supported the primary science mission objectives. A detailed tutorial video explaining the antenna arrangement, specular point sampling, and composite spatial coverage provided by the full CYGNSS constellation is available at [27]. A photograph of all eight spacecraft undergoing vibration testing in their prelaunch configuration and an artist's rendering of a single spacecraft on orbit are shown in Fig. 1. A detailed examination of the mission's spatial sampling properties is

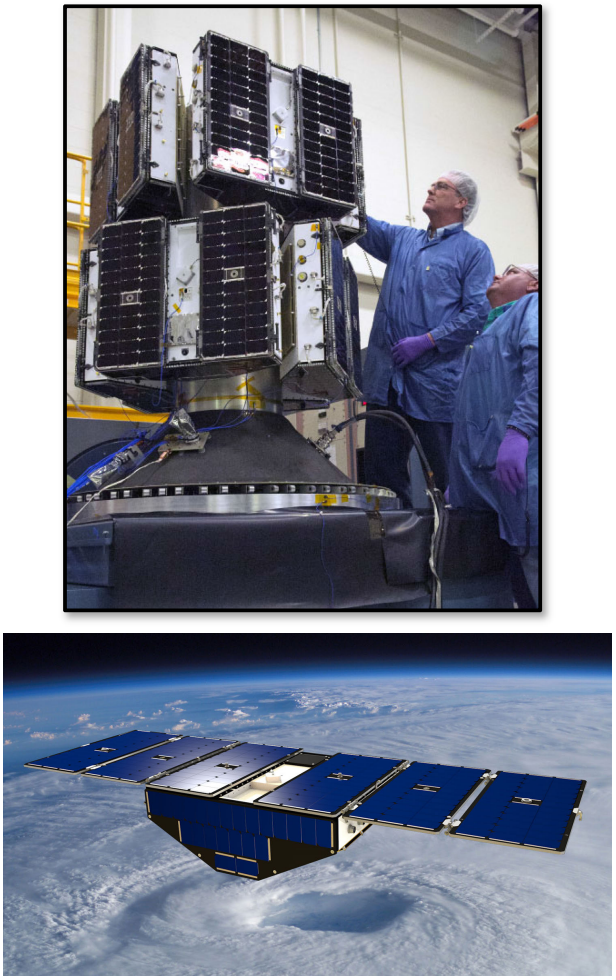


Fig. 1. *All eight CYGNSS spacecraft integrated on the central deployment module cylinder while undergoing prelaunch vibration testing (top). Artist's rendering of one of the spacecraft on orbit (bottom).*

provided in [28] and [29]. Unlike the TDS mission with its many shared payloads, CYGNSS was designed as a science mission dedicated exclusively to the operation of its DDMI payloads. The power, data handling, and downlink capacities of the individual satellites were all sized to support the continuous measurement of GNSS-reflected signals with a 100% duty cycle. Science operations began in March 2017 and continue to the present. As a result, CYGNSS provides the first comprehensive collection of DDM observations of the Earth from space [30]. A complete record of all science data products, including links to the data files for the entire mission, is available in [31].

C. Follow-On GNSS-R Missions

Following the successful demonstration by CYGNSS that stable, well-calibrated geophysical measurements could be made from space by GNSS-R remote sensing, a confluence of circumstances led to a proliferation of other GNSS-R missions. GNSS-R receivers have become smaller, lower power, and cheaper to manufacture as a result of the rapid expansion of low-cost commercial cellular and GNSS electronics. The antennas required of a GNSS-R sensor are also both smaller and cheaper to manufacture than those used by traditional spaceborne radars and microwave radiometers. As a result, both the receiver and antenna are of a sufficiently small size, weight, and power that they can be accommodated on modest microsats and cubesats. Two other enabling technology expansions also occurred at the same time, those of miniaturized satellites and low-cost launch vehicles. The relative ease of access to space combined with the reduction in size and cost of satellites resulted in a marked increase in the number and level of activity of national government space agencies and of smaller private sector "New Space" companies. As these organizations consider possible environmental sensing payloads to fly, GNSS-R has become an attractive option.

Several government space agencies have either launched new GNSS-R missions or confirmed missions that are currently in prelaunch development. The Bufeng-1A/B pair of satellites was launched on June 5, 2019, by Chinese Academy of Space Technology [32]. Each satellite carries a GNSS-R payload, and the mission has produced a range of well-calibrated geophysical data products [33]. A constellation of Fengyun-3 satellites (FY-3E/F/G) was launched by Chinese Meteorological Administration in 2021 and 2023, carrying GNSS-R payloads to be used operationally by numerical weather prediction models [34], [35]. The TRITON satellite, built by Taiwanese Space Agency, launched on October 8, 2023, carrying a GNSS-R payload to support the study of Typhoon physical processes and numerical weather prediction [36]. The ESA CubeSat mission PRETTY was launched together with TRITON and also carried a GNSS-R payload [119]. ESA is currently preparing the HydroGNSS satellites for launch later in 2025. They carry an upgraded version of the GNSS-R payload flown on the CYGNSS satellites, both of which were developed by SSTL [37].

Commercial development of follow-on GNSS-R satellites has proceeded in parallel with the government missions. Spire Global began launching its series of cubesats carrying GNSS-R payloads in 2018. There have been several "batches" of launches since then, each containing technological advances over the previous batch [38]. The Tianmu-1 constellation of GNSS-R satellites is being developed by Aerospace Tainmu Satellite Technology Company Ltd. They launched their first satellites in 2021, have had a number of subsequent launches, and the constellation currently numbers 23 operational GNSS-R spacecraft [39]. Muon Space has also developed a GNSS-R payload, based in part on CYGNSS technology licensed from the University of Michigan [40], and its first GNSS-R satellite, MuSat-2, was launched in 2024 [41].

II. REVIEW OF GNSS-R CONCEPTS

The first step in understanding GNSS-R is an understanding of the underlying technology of the GPS (the most

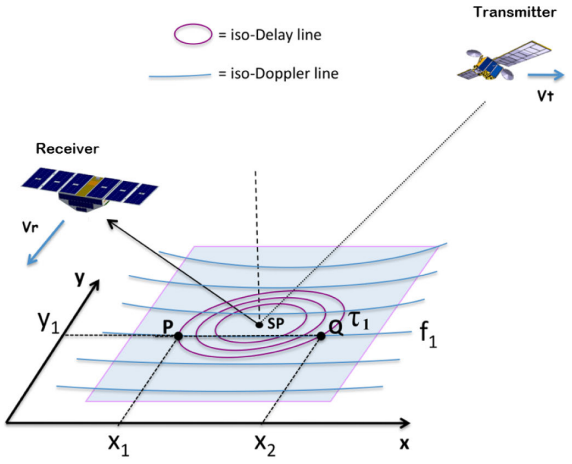


Fig. 2. ***GNSS-R measurement geometry. Angles of incidence and reflection are equal at the specular reflection point (SP). The propagation time from transmitter to surface to receiver is also minimized at the SP. The locations of reflections at longer times are shown as iso-delay ellipses. The GNSS signal is Doppler-shifted by the relative motion between transmitter and receiver. Shifts above and below that at the SP are shown as iso-Doppler lines. A mapping exists from spatial coordinates (x, y) to (delay, Doppler) coordinates (τ, f) with some ambiguity, as in P and Q mappings to the same (τ1, f1) values.***

established GNSS) and traditional GPS receiver signal processing algorithms. Good fundamental references with regard to the GPS constellation and GPS receiver design include [42] for a thorough overview of GPS signals and receivers, as well as [43] or [44] for comprehensive summaries on a wide range of GPS principles and applications, [45] for specific application chapters and open-source code on GNSS remote sensing (including UK-DMC data), and [46] for valuable descriptions of combined GNSS systems and receiver designs. Summaries of the main GNSS system and receiver components are included in the following. The basic reflection geometry of a GNSS-R observation is shown in Fig. 2.

A. GNSS System and Receiver Overview

There are currently multiple operational GNSS constellations, all of which consist of numerous satellites. Each transmits several navigation signals at different frequencies and with different code/carrier modulation designs. These constellations include GPS (operational since 1995 [45]), European Galileo constellation, Russian GLONASS constellation, as well as newer constellations coming online such as Chinese BeiDou system. GNSS satellites are normally in medium Earth orbit (the orbit periods of the largest GNSS constellations are: GPS ∼11 h 58 min, Galileo ∼14 h, GLONASS ∼11 h 16 min, and Beidou ∼12 h 40 min) and for complete Earth coverage number 24 or more satellites operating continuously (although constellation sizes vary). In addition to the main GNSS satellite transmitters, satellite-based augmentation systems (SBASs) transmit similar signals, usually in geosynchronous orbits, which are often used to augment navigation accuracy for a given constellation (for example, WAAS for GPS and EGNOS for Galileo).

Each GNSS satellite transmits multiple signals at several frequencies and with different modulation schemes. For example, early GPS satellites transmitted at two frequencies ($L1$ and $L2$) with independent, orthogonal signals (one civil and one military) that are phase-modulated together at a given carrier frequency. Many traditional receivers use two frequencies together to correct for ionospheric errors during position estimation [45]. Later, GPS satellites included a third frequency ($L5$). From a remote sensing perspective, there are two primary considerations when using a reflected GNSS signal to observe the surface: the carrier frequency and the code modulation design. For all GNSS constellations, the transmitted carrier frequencies vary slightly, but all reside in L band. This is a key advantage in some regards (it provides robust penetration of clouds, rain, and vegetation), but operation at L band is not standard for some applications and can require additional development of physical models and retrieval algorithms. For example, ocean surface winds and sea surface height (SSH) are more often sensed using higher microwave frequencies, so the existing scattering models and retrieval algorithms have been tuned to work best there. In the case of land soil moisture sensing, L band is the preferred frequency range of many traditional soil moisture-sensing instruments (e.g., SMAP and SMOS). The second key characteristic is the code modulation scheme. GNSS systems are designed with a spread-spectrum technique that modulates a pseudorandom code (of varying length, depending on the signal) on the carrier that needs to be known in the receiver to despread the signal (i.e., narrow the bandwidth with coherent correlation) to be able to detect and track the transmitted signal. For example, the GPS $L1$ *C/A* signal (the most commonly used for navigation and GNSS-R) uses 32 unique 1-ms spreading codes of 1024 1-μs "chips" (not "bits," as they contain no data), one for each transmitter (although codes can be reused as old and new satellites go off or come online). A typical GPS receiver internally stores these 32 codes and searches through its received signal, coherently correlating over 1-ms intervals to find and track the transmitting satellites in view. When four or more satellites are acquired and tracked by a receiver, the received signal itself is used to both make range measurements and provide demodulated navigation data (on timing and transmitter position) to allow the receiver to estimate its position, velocity, and time (PVT).

GNSS signals, such as GPS $L2$/$L5$ and Galileo E1/E5, are all slightly different and each has its own advantages and disadvantages for GNSS-R. For example, GPS $L5$ has a 10× faster chipping rate (10 230 chips/ms), providing much finer potential surface resolution, but it also shrinks the reflecting surface glistening zone, reducing the power received, making its GNSS-R utility still an open question.

B. Coherent and Incoherent Link Equations

GNSS-R surface reflections can be classified into two broad categories, with the possibility of mixing between the two types of reflections possible under certain surface conditions. The dominant reflection type over the ocean involves diffuse scattering, usually when winds are greater than ∼5 m/s, which is the large majority of the time. The diffuse scattering case described in the Zavorotny and Voronovich [8] model assumes that numerous small reflecting surfaces return power toward the receiver over a large extent of the surface glistening zone. This is due to the variations in orientations of the surface, resulting in a distribution of reflected power toward the receiver. The underlying cause of diffuse surface scattering is a complicated interaction of the statistical distribution of surface heights and the orientation of the reflecting surfaces toward the receiver over the entire glistening zone (tens of km^2), and specifically over the first Fresnel zone for a given incident wavelength (see Section III-D) [47]. However, a general rule as to when the surface is sufficiently rough to result in diffuse scattering is the Rayleigh criteria, stating that if the height differences on the surface are more than the $\lambda_{\text{GNSS}}/[8\sin(\theta_{\text{grazing}})]$, within the first Fresnel zone, then diffuse scattering will dominate. This effectively results in incoherent scattering, which can be roughly thought of as a "retransmission" from the surface. This results in the power at the receiver being described as a function of delay and Doppler by the following link equation, based on the traditional bistatic radar equation but modified in [8] to account for the GPS signal delay and Doppler responses (taken from [48]):

$$P^g(\tau,f) = \frac{P^T\lambda^2}{(4\pi)^3}\iint_A \frac{G^T\left(\vec{r}\right)\sigma^o\left(\vec{r}\right)G^R\left(\vec{r}\right)}{\left(R^T\left(\vec{r}\right)\right)^2\left(R^R\left(\vec{r}\right)\right)^2}\Lambda^2(\tau;\vec{r})S^2(f;\vec{r})d\vec{r} \tag{1}$$

where P^g is the coherently processed scattered signal power as a function of delay τ and frequency f. P^T is the GPS satellite transmit power, G^T is the GPS satellite antenna gain, G^R is the instrument receive antenna gain, R^T and R^R are the transmitter to surface and surface to receiver ranges, σ^o is the normalized bistatic radar cross section (NBRCS), λ is the GNSS signal carrier wavelength (∼19 cm for GPS $L1$), Λ and S are the GPS signal spreading functions in delay and frequency (also known as the Woodward ambiguity functions), and the double surface integral is over the effective region of diffuse scattering or glistening zone, A. The delay and frequency values, τ and f, map nonuniquely spatially to physical $\vec{r} = (x, y)$ coordinates on the surface, as illustrated in Fig. 2.

Alternatively, when the reflecting surface is relatively smooth with respect to the signal wavelength, a coherent surface reflection is possible. This can be visualized as the incident GPS signal reflecting from the surface as if it where a mirror. In this case, the power directed toward the receiver is given by [47]

$$P^g_{\text{SP}} = \frac{P^T G^T(\text{SP})G^R(\text{SP})\lambda^2\Gamma_{\text{SP}}}{(4\pi)^2\left(R^T(\text{SP})+R^R(\text{SP})\right)^2} \tag{2}$$

where Γ_{SP} is the surface reflectivity at the SP, and the other parameters are the same as in (1) but calculated only at the SP. Important differences to note between (1) and (2) include the following.

1) The scattering/receiving spheres (4π) are raised to the third power in the diffuse case (representing an additional "transmission" at the surface) while only a power of two in the coherent reflection case.
2) The diffuse scattering case is an integral over a region of the surface, which requires some simplifications when making actual observations, as opposed to at the specular point only.
3) In the diffuse case, the range terms are squared individually, while in the coherent case, the sum of the ranges is squared. This last difference results in coherent reflections having much larger received power levels than the diffusely scattered reflections, which has major benefits for land and ice applications where the surface conditions are often smoother and coherent reflections are more prevalent.

The third reflection case is a combined or "mixed" diffuse/coherent reflection. These conditions do exist, and a robust retrieval algorithm should be able to distinguish which regime dominates any given measurement, which will determine which retrieval algorithm is appropriate to use. There are several options for separating diffuse and coherent reflections, one based on the magnitude and shape of CYGNSS DDMs is documented in [50]. Approaches that use the reflected signal carrier phase have also had considerable success [51].

C. Open-Loop Tracking

Fig. 2 shows the basic reflection geometry of a GNSS-R observation. In the design of a complete GNSS-R receiver, the system needs to have accurate estimates of: 1) the PVT at the receiver itself (normally provided by the standard GPS navigation solution); 2) the positions and velocities of the GPS transmitters at the same time (provided by decoding the data on the GPS signals themselves, used during the receiver PVT estimation); and 3) the location of the surface specular reflection point. With these three inputs, it is possible to identify which GPS reflections are in-view (and in the higher gain footprint of the receiver's nadir-looking antenna) and how to center the DDM processing algorithms to capture the reflected signal power over the surface glistening zone. There are several ways to estimate the surface reflection point, with one method described in detail in [52], which computes the reflection location on the WGS-84 ellipsoid. Importantly, for land reflections, the

surface rises above the WGS-84 ellipsoid, and the surface elevation needs to be accounted for in the specular point calculation.

During the real-time operation of GNSS-R receiver, the navigation solution is combined with a computationally efficient specular point estimator to forward predict multiple surface reflection locations in delay and Doppler to generate the measurements to be sent to the ground for subsequent engineering calibration and science data product estimation.

D. Delay–Doppler Map

A typical GPS navigation receiver is primarily concerned with tracking the received signal carrier and code phase, so long as the signal magnitude is sufficiently high for use—the signal power fluctuations themselves are not that relevant (so long as the signals stay above the detection/tracking threshold). In contrast, a GNSS-R receiver uses the transmitted signal as a bistatic radar, and the received signal magnitude is often the primary signal property of interest. Additionally, how the power spreads in the time (delay) and frequency (Doppler) domains can also contain important remote sensing information.

A traditional GPS receiver uses three (or five) delay/lag correlators per signal in closed tracking loops (in frequency, delay, and phase) to provide precise measurements of the signal peak delay and phase (providing the fundamental range measurements used in navigation). In order to create a DDM of the signal spread over the surface, it is necessary for the receiver to observe the signal at numerous time delays and Doppler frequencies around the reflected signal center. In order to accomplish this, significantly more correlators are needed per surface reflection. For example, the DDM observations by CYGNSS are 11 Doppler bins (at 500-Hz spacing) and 17 delay bins (at 0.25 chip spacing), which is a cropped version of the 20 Dopplers by 128 delays of the instruments full processing capability. This excessively large delay and Doppler space is used to obtain a complete signal power mapping as well as to mitigate open-loop tracking errors, notably when the reflected signal is over elevated and rapidly varying terrain.

One of the fundamental observations made by a GNSS-R remote sensing receiver is the DDM at a geo-located specular reflection point on the surface. Both the magnitude of the received peak, as well as the power spreading in delay and Doppler, are the key metrics by which the surface conditions are estimated. An example DDM from CYGNSS captured over the ocean is shown in Fig. 3. The "horseshoe" shape is due to the reflected signal power distribution over a wide area of the "glistening zone" shown in Fig. 2.

These additional requirements for the reflection channels in a DDM receiver drive innovative algorithms and require additional hardware resources (in application-specified integrated circuit (ASIC) or field-programmable gate array (FPGA) capacity) to enable multiple parallel real-time surface observations at sufficient resolution for remote sensing. Notably, the instruments on CYGNSS and TechDemoSat were designed conservatively in this regard, where the actual retrieval algorithms often rely on a relatively small number of DDM pixels (typically, five Doppler $\times$ three delays for ocean sensing, and often only the signal peak for land soil moisture and surface water applications), making the standard DDM size versus the number of parallel observations for future instruments and missions an ongoing discussion (see Section VI).

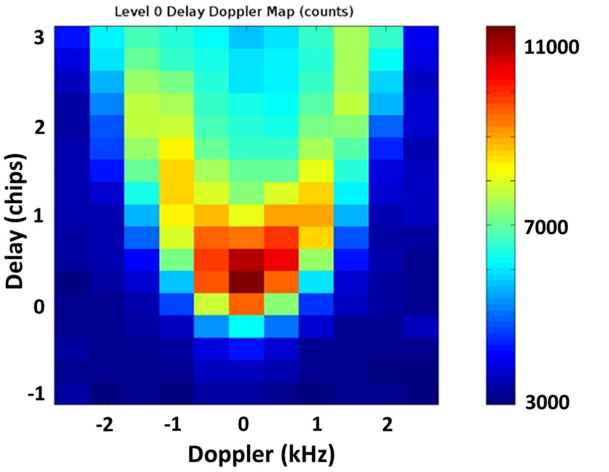


Fig. 3. *Example DDM measured by CYGNSS over the ocean. This is the standard (compressed and truncated) data product generated >99% of the time. Higher resolution versions are commanded over target areas of interest.*

Techniques for processing DDMs include: a frequency dimension fast Fourier transform (FFT) (also known as zoom correlator) [21] used in the CYGNSS instrument, a delay-domain FFT-based algorithm often used in signal acquisition [45], as well as traditional delay/Doppler correlator loops. A comparison of these techniques is included in [53].

III. CALIBRATION OF LEVEL 1 ENGINEERING DATA PRODUCTS

The initial step in the calibration of DDM measurements is the conversion of the Level 0 DDM to received power, which is recorded as raw signal counts, into engineering units of power (W) [54], [55]. The second step is the conversion of the area of interest in the DDM (generally the region around the specular point peak) into an NBRCS measurement [47], [55] or a measurement of surface reflectivity [49]. The NBRCS is the primary measurement over ocean surfaces and diffuse scattering conditions. Surface reflectivity is the relevant observation in the case of predominantly coherent reflection from the surface, which occurs more frequently over land and sea ice. The models for these measurements are presented in (1) and (2), respectively. Inverting these models to solve for the

appropriate surface parameter, as well as discussions of surface resolution, is summarized as follows.

A. Calibrating Level 0 DDMs to Received Power

For the sake of this discussion, we follow the NASA CYGNSS product naming conventions. The DDMs generated by the instrument are considered the Level 0 data product. This consists of the raw uncalibrated DDM counts as generated by the instrument processor, as well as metadata (i.e., satellite position, velocity, physical temperatures, etc.). Initially, the DDM is converted to units of power as the Level 1a product. In order to provide a physical power reference within the instrument, the receiver input is periodically switched from the science antennas to a "blackbody" calibration load (nominally a 50-Ω resistor) that is temperature-monitored. The instrument switches to these loads for several seconds every 10 min based on the observed thermal dynamics of the hardware. By knowing the temperature of the blackbody load and the bandwidth of the signal, it is possible to calculate a physical power reference ($P_B = kTB$) for every DDM. This reference is used to convert the Level 0 count DDM to a Level 1a power DDM according to

$$P^g(\tau, f) = \frac{(C(\tau, f) - C_N)(P_B + P_r)}{C_B} \tag{3}$$

where C is the total counts at each delay and frequency pixel (τ, f) of the processed DDM, and C_N is the counts in a noise-only area of the DDM (located at shorter delay pixels above the surface where no reflected power is present). The signal-only counts in each DDM pixel are then scaled by the blackbody load power (P_B, observed during the calibration load switch and interpolated to the measurement epoch), the instrument thermal power (P_r) that is determined using a lookup table determined prior to launch which characterizes the receiver noise power as a function of temperature, and the observed blackbody counts (C_B). The result is a Level 1a DDM of received signal power over all DDM delay and Doppler pixels.

B. Normalized Bistatic Radar Cross Section

The measured signal power resulting from the Level 1a calibration is then used to determine the surface NBRCS by algebraic manipulation of (1). A number of simplifications are made to enable efficient calculation of NBRCS in the near-specular reflection area. These include: 1) eliminating the surface integration across the entire DDM in favor of discreet mean values in the area of the specular reflection point (the center of the DDM) and 2) normalizing the bistatic radar cross section by a single near-specular area region. In this case, the near-specular DDM area (DDMA) is defined as a 5 Doppler $\times$ 3 delay pixel area around the peak of the Level 1a DDM. With these simplifications, we can invert the observation model (1) to isolate the NBRCS (σ^o) over a limited region around the specular reflection point

$$\sigma^o_{\text{DDMA}} = \frac{P^g_{\text{DDMA}}(4\pi)^3 \left(R^T_{\text{SP}}\right)^2 \left(R^R_{\text{SP}}\right)^2}{P^T \lambda^2 G^T_{\text{SP}} G^R_{\text{SP}} A_{\text{DDMA}}} \tag{4}$$

where P^g is the Level 1a calibrated power summed over the DDMA pixels, P^T and G^T are the GPS transmitter power and antenna gain, respectively, R^T and R^R are the transmit and receive propagation ranges to the specular point, respectively, G^R is the receiver antenna gain, A is the effective scattering area corresponding to the DDMA pixels, and λ is the GPS signal wavelength. Importantly, the physical scattering area needs to be converted to an effective scattering area to account for the spreading effects of the GPS signal modulation functions [54].

With an estimate of the NBRCS in the specular reflection point region, and reasonable assumptions regarding the presence of diffuse scattering (i.e., typical ocean conditions), the Level 1b NBRCS observations are used to estimate surface parameters such as ocean waves (mean-square wave slopes) and near surface wind speed, as described in Section IV.

C. Reflectivity

In the case of a coherent surface reflection, the primary observable is surface reflectivity. We invert the coherent signal model (2) to isolate the main observable, giving

$$\Gamma_{\text{SP}} = \frac{P^g_{\text{SP}}(4\pi)^2 \left(R^T_{\text{SP}} + R^R_{\text{SP}}\right)^2}{P^T \lambda^2 G^T_{\text{SP}} G^R_{\text{SP}}} \tag{5}$$

where P_g is the Level 1a calibrated power at the DDM specular point pixel. P^T, G^T, and G^R are again the transmitter and receiver power and antenna gains, respectively, while the range loss terms are added and squared as per the coherent reflection condition. At this point, the estimates of the Level 1b reflectivity can be input into Level 2 surface retrieval algorithms to estimate geophysical properties such as surface water and soil moisture.

D. Spatial Resolution

The requirement for the surface spatial resolution in the diffuse NBRCS case was demonstrated for CYGNSS soon after launch in [29], which demonstrated that the surface resolution is on the order of 15–25 km, increasing with the incidence angle of the scattering geometry. The resolution of a DDM observation from LEO for the case of diffuse scattering is determined by the "chipping" rate of the reflected GNSS signal, the extent of the DDM region used in the geophysical parameter retrieval, the reflection geometry of the receiver (i.e., the altitude above the surface), the GNSS spreading functions [see (1)], and the noncoherent averaging duration. An analysis of the surface resolution of DDM observations can be found in [56] and [57].

As an example, for a GPS $L1$ *C/A* reflection (i.e., CYGNSS), the length of a single code chip is approximately 293 m, which, when mapped over the surface as observed from 500-km altitude, extends over multiple square kilometers of surface. The convolution with the GNSS ambiguity function causes additional spreading as the power is correlated across $+/-1$ μs of surface delay space. Illustrations of DDM surface mapping are presented in [25] and [26]. The DDMA region discussed above, which is used in the standard CYGNSS ocean observations, includes three delay bins (at 0.25 chip spacing) extending over a total of 0.25 chips ahead of the specular point. The result is the constraining of the surface power received to within the desired extent (in the case of CYGNSS, 25 km^2 or less). Additional regions of the DDM can be included to capture more reflected power at the expense of degrading the surface resolution, as described in [57].

One additional consideration is the duration of the noncoherent averaging interval. This is nominally 0.5 or 1 s, but can be less. During this averaging interval, the DDM specular point moves across the surface, thus increasing the surface resolution (the 0.5 s of averaging for a CYGNSS DDM results in roughly 3–4-km movement over the surface during its processing). This results in a "smearing" of the instantaneous resolution along the surface.

The surface resolution in the coherent reflection case is determined by the size of the first Fresnel zone at the signal carrier frequency. The coherent reflection on the surface is from a significantly smaller region, determined by traditional reflection theory and the wavelength of the incident radiation ($\lambda = 19$ cm for the case of the $L1$ carrier). The first Fresnel zone diameter is on the order of one kilometer for typical space-based geometries and varies with the incidence angle of the reflection. For example, for typical CYGNSS measurement geometries, the first Fresnel zone is a circle with a diameter of $\sim$600 m at nadir (0° angle of incidence) and grows to a 950 $\times$ 2300 m ellipse at 65° [49], [58], [59].

IV. RETRIEVAL OF LEVEL 2 SCIENCE DATA PRODUCTS

The Level 1 ($L1$) engineering measurements made by a DDM sensor are the NBRCS (σ^o) over rougher surfaces when incoherent scatter is dominant and the reflectivity (Γ) over smoother surfaces that support coherent reflection. Level 2 science data products are derived from the $L1$ measurements by identifying the physical properties at the surface that affect the engineering measurements, developing a forward model that predicts the measurements given the surface conditions, and then inverting the forward model to estimate a physical property from the measurements. The process for inverting the forward model is generally referred to as the retrieval algorithm. Examples follow of the primary surface properties that are retrieved from GNSS-R measurements. Most ocean measurements are consistent with incoherent scattering conditions due to the typical roughness properties of a wind-driven ocean surface. Most land measurements are partially coherent, with the coherent portion of the scattered signal being the dominant contributor to the received power. As a result, ocean science data products are typically derived from measurements of σ^o, whereas land science data products are derived from measurements of Γ.

A. Ocean Surface Wind Speed

The NBRCS of the ocean surface is related to its surface conditions by [8]

$$\sigma^o = \frac{|R|^2}{\text{MSS}} \tag{6}$$

where σ^o is the NBRCS, R is the Fresnel reflection coefficient of the smooth ocean surface, and MSS (also known as mean square slope) is the mean of the square of the slope of the surface height, where the mean is an expectation over the probability distribution of the surface roughness. In practice, MSS is most often computed in the spectral domain as the second moment of the ocean height roughness spectrum with respect to wavenumber [9]. Notably, the ocean roughness spectrum is affected by wind stress driven by near-surface winds. It is the connection that allows the wind speed to be retrieved from measurements of σ^o over the ocean.

A quantitative relationship between σ^o and near-surface wind speed is represented by a GMF. The GMF used by the CYGNSS wind speed retrieval algorithm is generated empirically from a large collection of CYGNSS measurements of σ^o, which are coincident with ocean wind speed at 10 m height above the surface reported by European Centre for Medium-Range Weather Forecasting reanalysis model version 5 (ERA5). An example of the GMF used by the CYGNS $L2$ wind speed retrieval algorithm is shown in Fig. 4. Several properties of the relationship between wind speed and σ^o are evident. There is only a weak dependence on the incidence angle of the scattering geometry. The NBRCS decreases monotonically with increasing wind speed. And there is a marked and rapid increase in NBRCS at very low wind speeds. This last property is an indication of the transition from incoherent to coherent scattering as the ocean surface becomes very smooth at low wind speeds.

Wind speed is estimated from measurements of NBRCS using a tabulated version of the GMF as a lookup table. Secondary corrections are made to the estimate to account for other properties of the sea surface roughness that can also affect the MSS, namely, the significant wave height of the surface. A detailed description of the CYGNSS wind speed retrieval algorithm is described in [61], [62], and [63]. The quality of the retrieved wind speed can be characterized by comparisons with coincident estimates provided by the ERA5 reanalysis product. A large, global intercomparison dataset is used, consisting of all pairs of wind speeds during 2018–2023 that are coincident to

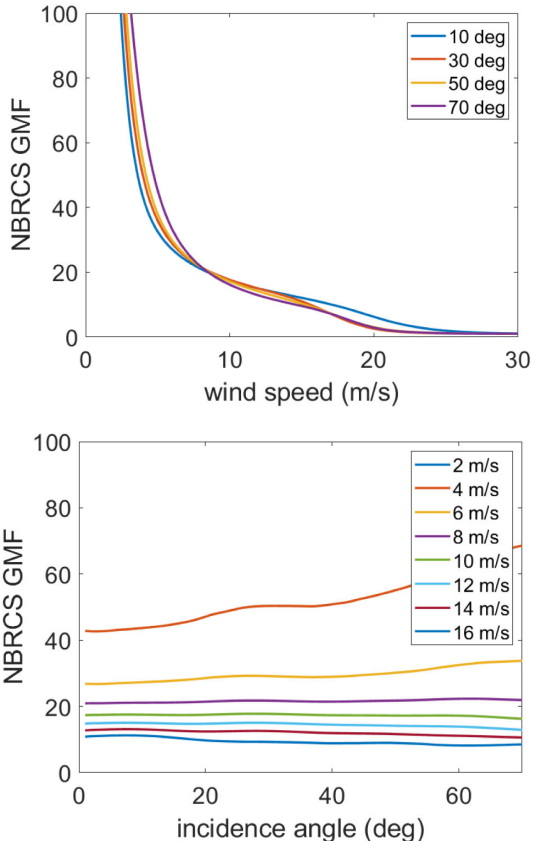


Fig. 4. *GMF mapping near surface ocean wind speed to NBRCS—used by the CYGNSS wind speed retrieval algorithm. The GMFs are plotted as a function of wind speed at different incidence angles (top) and incidence angle at different wind speeds (bottom) [60].*

within 60 min and 50 km [64]. A density scatterplot of the two winds is shown in Fig. 5(a), and the rms and mean differences between them as a function of the ERA5 wind speed are shown in Fig. 5(b). Overall, the root mean squared difference (RMSD) and bias between the CYGNSS and ERA5 winds are 1.7 and 0.1 m/s, respectively. Note in Fig. 5(b) that the RMSD begins to increase above ~10 m/s and continues to grow monotonically with increasing wind. This is an intrinsic property of wind speeds derived from DDM measurements that results from the increase in ocean surface roughness, the corresponding decrease in σ^o and received power, and the resulting decrease in signal-to-noise ratio (SNR) of the measurements as wind speed increases.

In very high wind conditions, and in particular in major organized (i.e., cyclonically rotating) storms, the relationship between σ^o and wind speed is altered by the limited fetch length and young sea state that are present, as compared to the fully developed seas (FDS) away from storms. As a result, a modified GMF is used to retrieve wind speed that is based on matchups between CYGNSS measurements in storms and coincident wind speed measurements made by hurricane hunter aircraft and National Hurricane Center forecast models. This process is described in [62]. The high and low wind versions of the retrieval, referred to as the FDS and Young Seas Limited Fetch (YSLF) wind speed data products, are then merged into a single product that selects the appropriate GMF and retrieval algorithm depending on the proximity to an organized storm [65]. An example of the global merged wind speed product produced by CYGNSS is shown in Fig. 6. In the figure, FDS winds are retrieved away from Hurricane Sam, YSLF winds are retrieved in and near the storm, and a tapered transition from one to the other is applied around the storm's perimeter.

B. Sea Surface Height

In addition to measuring near-surface winds over the ocean, GNSS-R measurements can also be used to measure the total propagation time of the reflected GNSS signal, from which SSH is found. The method is roughly analogous to a conventional radar altimeter, but there are significant differences in the satellite orbits and signal properties in the bistatic GNSS-R case that can make its

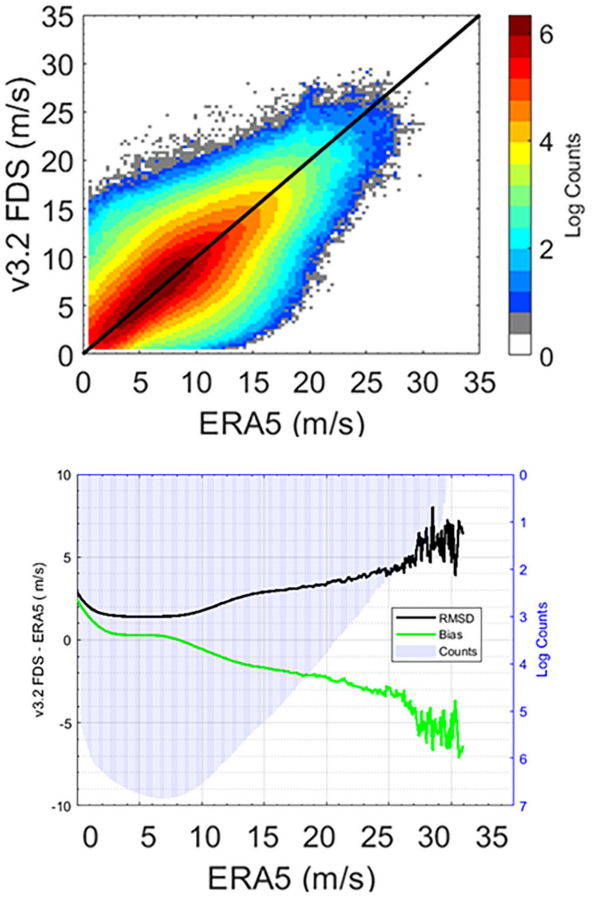


Fig. 5. *Log-density scatterplot between CYGNSS v3.2 wind speed and coincident ERA5 winds for all of 2018–2023 (top). RMSD and bias between the two wind speeds as a function of the ERA5 wind [64] (bottom).*

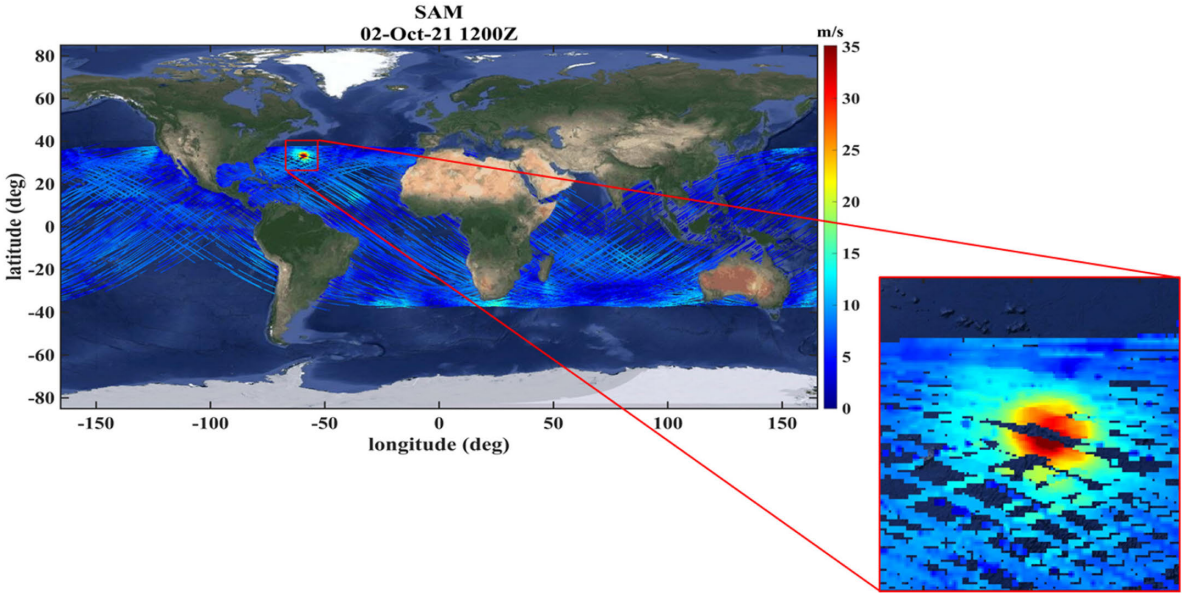


Fig. 6. *Composite of all CYGNSS wind speed measurements made by the eight satellite constellations during the period 0600–1800 Z on October 2, 2021. Hurricane Sam was active at this time in the West Atlantic, and the inset shows the winds centered on the storm.*

measurement of SSH more challenging. There are two methods for measuring the propagation time. Group delay altimetry performs a lag correlation of the received signal with a local replica of the pseudorandom number sequence that is modulated on the GPS carrier. This is equivalent to a range-gated radar, and the range resolution (and thus the SSH uncertainty) is inversely proportional to the bandwidth of the modulation. Given the modulation applied to GPS signals, the SSH uncertainty is on the order of meters. Examples of successful spaceborne GNSS-R group delay altimeters are presented in [66] and [67]. An alternative approach is the carrier phase altimetry, which strips the modulation from the GNSS carrier signal and then estimates its phase. In this case, the range uncertainty is limited by the quality of the phase determination, which is, in turn, dependent on the SNR of the received signal. An example of successful spaceborne GNSS-R carrier phase altimetry is presented in [68], with a phase error of order 45° (1/8 cycle) and a corresponding precision in range determination of $\lambda/8 = \sim$3 cm. Note that this is only the precision of the GNSS-R range determination. A number of other propagation dependencies must be corrected to determine absolute SSH. While carrier phase altimetry has inherently better measurement uncertainty, it can only be performed if the carrier is recoverable. This typically requires a very smooth ocean surface consistent with calm seas and little swell. In practice, sufficiently smooth conditions happen only infrequently.

C. Soil Moisture

The power received by a GNSS-R sensor due to specular reflection from a smooth, flat surface is given by (2). The reflectivity term, Γ, is the Fresnel reflection coefficient, which depends on the dielectric properties of the surface. For most soils, the strongest determiner of its dielectric constant is its volumetric moisture content. This is the physical basis for the sensitivity of DDM measurements to soil moisture. In practice, land surfaces are not perfectly smooth, and they are sometimes covered by a vegetation canopy. To account for this, the idealized Fresnel reflectivity of a smooth, flat surface (Γ) can be replaced in (2) by an effective reflectivity, given by

$$\Gamma_{\text{eff}} = \Gamma \exp\left(-(2kh\cos\theta)^2\right) \exp\left(-2\tau\sec\theta\right) \tag{7}$$

where $k = 2\pi/\lambda$ is the wavenumber ($\lambda = 19$ cm for the GPS $L1$ carrier), h is the rms height of the rough surface, θ is the incidence angle of the reflected signal, and τ is the optical depth of the vegetation canopy [69].

Soil moisture retrieval algorithms from GNSS-R measurements use several different approaches. Regression-based algorithms assemble a large dataset of observations of Γ_{eff} and coincident measurements of soil moisture, to which an analytical expression is fit using least-squares techniques. The dataset is often subdivided into smaller localized subsets prior to the regression to account for variations in surface roughness and vegetation. Examples of this regression-based approach are provided in [70] and [71]. Another retrieval approach is the inversion of a semiphysical forward model. In this case, a parameterized forward model is first developed, in which adjustable parameters of the model are determined from a coincident dataset of DDM observations and soil moisture measurements. This forward model is, then, inverted mathematically. An example of this approach to GNSS-R soil moisture retrieval is given by Kim and Lakshmi [72]. A third

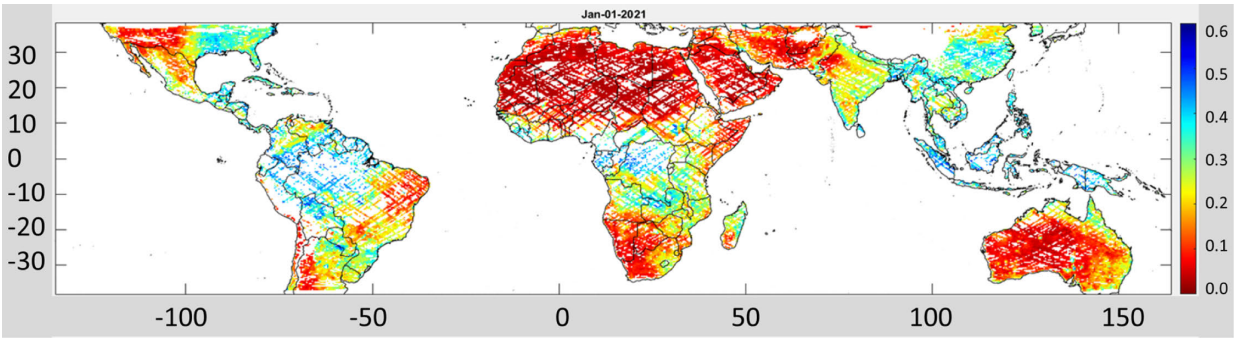


Fig. 7. ***Volumetric soil moisture content retrieved by the CYGNSS constellation over a 24-h period on January 1, 2021, based on the v3.2 project science data product [75].***

approach also begins with a large dataset of coincident DDM and soil moisture data and uses it to train a neural network estimator of soil moisture given Γ_{eff}. Examples of this approach are provided by Eroglu et al. [73] and Setti and Tabibi [74]. The CYGNSS Mission produces a global soil moisture map using a regression-based approach. An example of its daily data product is shown in Fig. 7.

D. Inland Water Mapping

While GNSS reflections from land tend to be partially coherent with a stronger coherent component, the reflections from inland water bodies tend to be highly coherent due to the smooth surfaces typical of lakes and rivers. In this context, a surface is smooth if its rms roughness is a small fraction of the 19-cm wavelength of the GPS signal being observed. In addition, the dielectric contrast between air and water is much greater than that of air and soil (even when moist), which results in a larger Fresnel reflectivity. For these two reasons, GNSS-R measurements are particularly sensitive to the presence of inland water. In practice, the reflectivity of land is typically ∼100 times weaker than that from inland water. Additionally, the spatial resolution of GNSS-R measurements collapses from tens of kilometers for a fully incoherent rough surface to hundreds of meters for a fully coherent smooth surface. The stronger reflected signal and better spatial resolution make GNSS-R a particularly attractive method for inland water detection and mapping. These properties of coherent GNSS-R reflections were well-understood prior to the launch of CYGNSS. What was not appreciated until its global, high-density measurements began to be analyzed was the likelihood with which inland water bodies support fully coherent reflection. It is in fact very rare for inland lakes, rivers, flood zones or inundated wetlands to have a surface rms roughness in excess of a quarter of the 19-cm GPS wavelength, which corresponds to a 10-m referenced wind speed of 3–4 m/s.

Early examples of the unique ability of GNSS-R to map land inundation by water are provided in [76], [77], and [78]. These demonstrations were followed by the development of an operational data product that produces three-day and monthly global water masks with $0.01^\circ \times 0.01^\circ$ spatial resolution. The product combines CYGNSS DDM observations with a computer vision algorithm to segment the images between standing water and dry land [79], [80]. An example of the monthly water mask is shown in Fig. 8.

In addition to the mapping of extended inland water bodies, GNSS-R can also detect and characterize smaller rivers. This ability derives from the fact that, while the spatial resolution of GNSS-R reflections from smooth surfaces is hundreds of meters, the strength of the reflection from water is so much stronger than that from land that even smaller rivers are easily detectable. Two applications of this

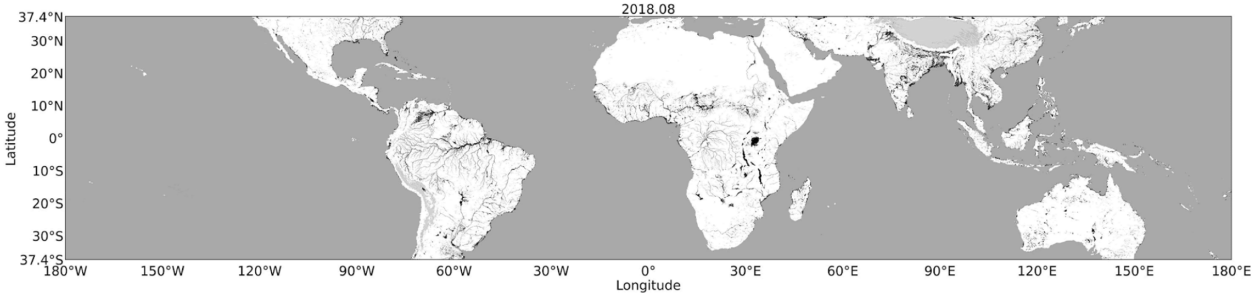


Fig. 8. ***Monthly CYGNSS water mask for August 2018. Inland water extent can be detected and mapped day or night, through clouds and precipitation, and under vegetation canopies [81].***

capability have been developed. One is the determination of river width and, indirectly, of river stream flow rate, using observations of specular point track river crossings [82]. Uncertainties in river width determination of tens of meters are possible due to the much stronger reflection from water than land [83]. The other application is the determination of river slope from the analysis of specular point tracks that run parallel to the river [84]. In this case, carrier phase altimetry is used to determine the relative height along the river surface, and changes in the height determine the slope. Slope uncertainties of 0.4 cm/km have been reported [85].

E. Freeze/Thaw State

The phase change of water from liquid to solid is accompanied by a large change in its dielectric properties at microwave frequencies. Given the sensitivity of GNSS-R land reflections to the dielectric constant of the surface, this provides another remote sensing application—the determination of the freeze/thaw state of the surface. Thresholding algorithms have been developed to reliably predict the F/T state [86]. They can, then, be applied to repeat observations of the same region to resolve its spatial and temporal dynamics, with applications in water resource management, permafrost trends, and wildfire risk assessment. One example is shown in Fig. 9, of the spatial distribution of first thaw date in the spring and first freeze date in the fall across the Tibetan Plateau derived from CYGNSS observations [87].

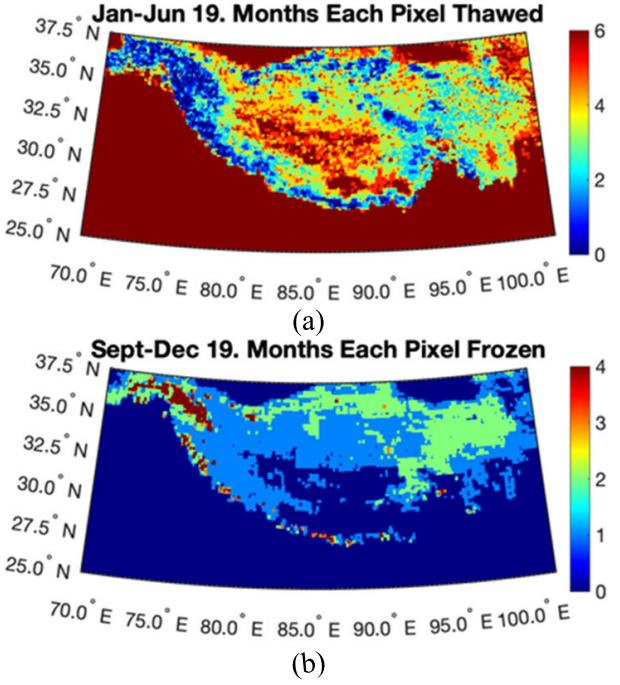


Fig. 9. *CYGNSS spring thaw and fall freeze dates for 2019 over the Tibetan Plateau. The first month of spring with a thawed surface state is shown in (a), and the first month of fall with a frozen surface state is shown in (b) [87]. The color scale refers to the fractional month: (a) January–June and (b) September–December.*

V. EXAMPLES OF SCIENTIFIC APPLICATIONS

The first well-sampled spaceborne DDM data products became available in 2017. Scientific applications of the data are just beginning to be explored by the many communities of end data users as they become accustomed to its unusual spatial sampling properties and they begin to make use of its unique remote sensing capabilities—namely, the ability to measure ocean winds under high levels of precipitation, the ability to resolve inland water bodies under clouds, precipitation, and vegetation canopies, the ability to detect and map small inland water bodies, and the ability, with a sufficiently large constellation of satellites, to track the diurnal behavior of weather systems and the short timescale dynamics of extreme weather events. Some of the early successful applications are summarized here.

A. Hurricane Forecasting

CYGNSS wind speeds have been assimilated into numerical weather prediction models to examine their impact on forecast skill for tropical cyclone track and intensity and tropical convection using: 1) the National Center for Environmental Prediction (NCEP) gridpoint statistical interpolation (GSI)-based hybrid 3D-EnVAR and 4D-EnVAR data assimilation systems [88], [89] and 2) the weather research and forecasting (WRF) model optimized for hurricane applications (HWRF) [90]. Comparisons between the predictions using only standard operational input data sources versus using the operational sources plus CYGNSS winds demonstrate that there is a significant positive impact on forecast skill provided by the GNSS-R winds.

B. Tropical Weather System Processes

The fact that GNSS-R measurements of ocean surface wind speed are not affected by precipitation that makes them a useful tool for studies of the physical processes associated with mesoscale convective systems (MCSs). Surface sensible and latent heat flux (SHF and LHF) products have been developed using CYGNSS observations of winds to support these studies [91]. SHF and LHF from the tropical and subtropical oceans have an important effect on the development of weather systems across a wide range of scales. This is the case for organized convective systems (including tropical cyclones) and for extratropical cyclones that form in the lower middle latitudes [92], [93], [94]. Much of the precipitation in the tropics is produced by MCSs that are not associated with tropical cyclones. They also play a key role in the formation and propagation of the Madden–Julian oscillation (MJO), which influences the variability of rainfall over much of the tropical western Pacific Ocean as well as the coasts of North and South America. The MJO also affects the genesis of tropical storms in the Pacific Ocean and Caribbean Sea. As such,

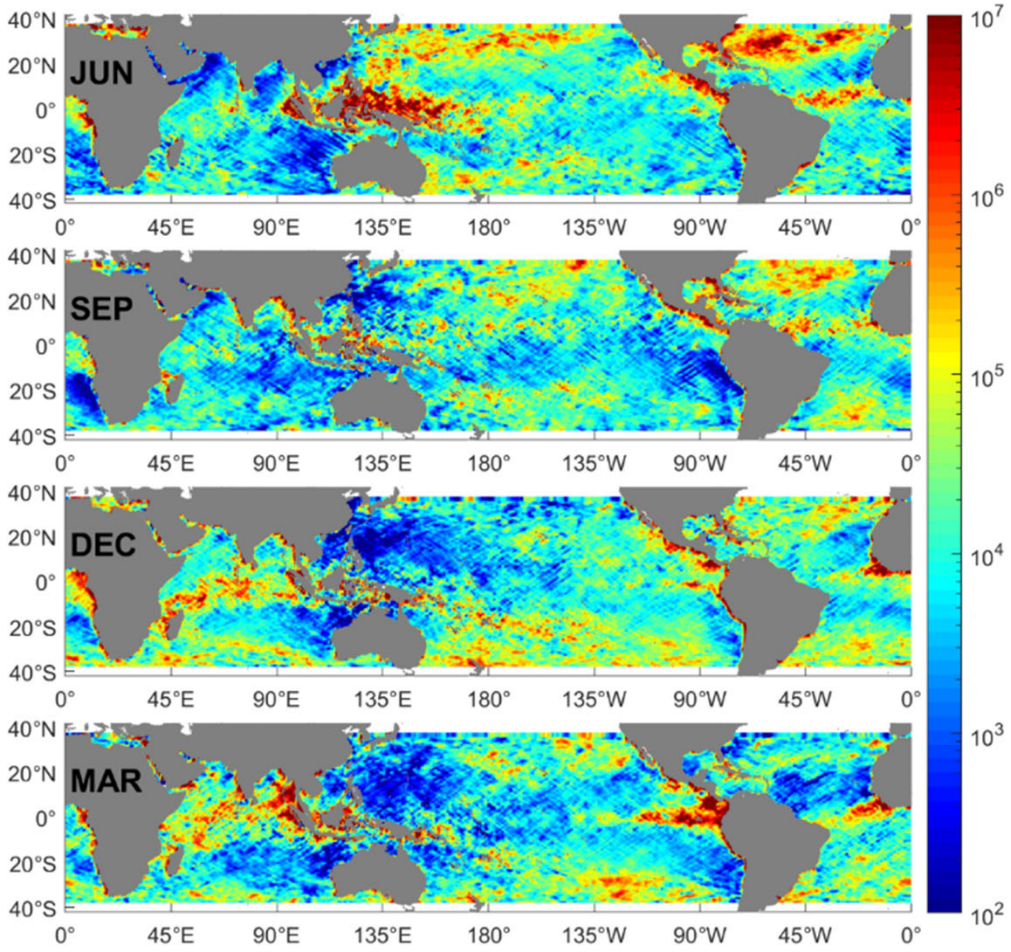


Fig. 10. *Monthly average microplastic number density concentration (#/km^2, log10 scale) for June–September–December 2017 and March 2018. Both Atlantic and Pacific basins have generally higher concentrations in austral and boreal summer. The northern Indian Ocean has the highest concentrations in the spring. These seasonal patterns are found to repeat annually [99].*

the MJO influences global medium and extended range forecasts and the prediction of precipitation. Previous measurement systems were capable of characterizing the thermodynamic environment and rain rate associated with the MJO, but GNSS-R adds significant new information about the surface winds and associated heat fluxes [95], [96], [97], [98].

One other application of CYGNSS ocean measurements derives from its sensitivity to the suppression of wind-driven ocean roughening caused by the presence of surfactants on the surface, which can act as tracers for the global distribution of ocean microplastics. This correlative relationship has been leveraged to produce the first global maps of ocean microplastics derived from spaceborne remote sensing observations [99]. Examples of monthly average ocean microplastic number concentration, derived from CYGNSS observations, are shown in Fig. 10.

C. Seasonal Wetland Inundation

In the tropical wetlands, large seasonal and interannual variations in wetland inundation levels are driven by wet/dry season dynamics, and inundated areas are often masked by extensive vegetation canopies and cloud cover that obscures visible or near-IR remote mapping methods. This leads to inaccurate, poor spatially and temporally resolved inundation maps and becomes a large fundamental gap in the representation of wetland methane emissions. CYGNSS-based inland water masks have the ability to significantly improve upon the traditional Vis/IR-based approaches. Fig. 11 shows examples of CYGNSS water masks over the Pantanal region of South America during dry and wet portions of the annual monsoon cycle. The Pantanal is the largest wetland area in the world.

Wetland extent is a primary contributor to the seasonal variability of global methane emission. The WetCHARTS methane emission model is a widely used reference for estimating the dependence of emission on wetland extent [100], [101]. The model has previously relied on either rainfall data or Vis–IR-derived maps with low seasonal variability to determine wetland extent. As illustrated in Fig. 12, the use of a CYGNSS-derived water mask instead of the SWAMPS [121] or ERA5 [122] wetland extent products significantly improves WetCHARTS correspondence with observations by the GOSAT and TROPOMI

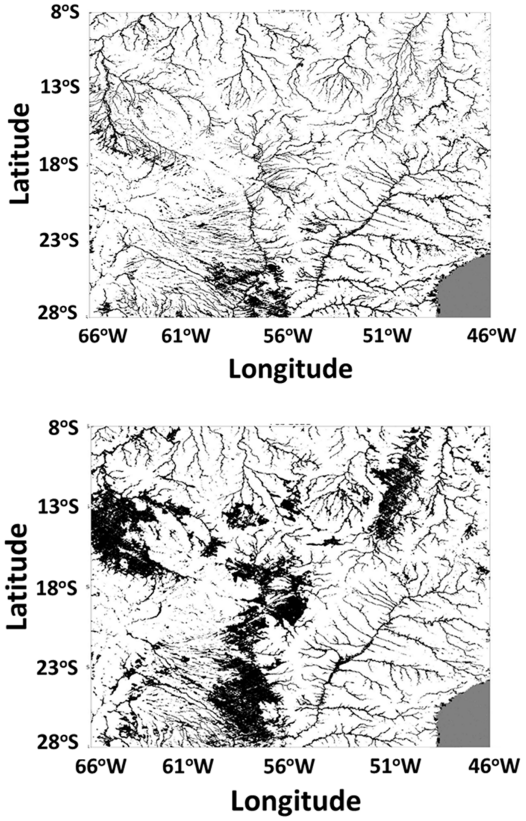


Fig. 11. *Monthly CYGNSS water masks of the Pantanal area for a dry month (top) and a wet month (bottom) [102].*

methane-sensing satellites, in terms of both the peak magnitude and the seasonal dependence [102]. CYGNSS observes a larger wetland extent during the monsoon season because of its ability to penetrate through clouds and rain. Water masks derived from Vis–IR observations cannot track the seasonal variability and tend to be biased toward the drier seasons.

VI. TECHNOLOGY ADVANCES

A. Dual-Polarization Measurements

The bistatic radar receivers used by CYGNSS and other GNSS-R missions (e.g., UK-DMC, TDS, and TRITON) operate with a single polarization. The transmitted GNSS signal is assumed to be purely right-hand circular polarized (RHCP), and the GNSS-R antenna receives only the LHCP component of the signal scattered by the surface. This is generally considered the co-pol component of scattering because it is dominant at lower incidence angles and with smoother surfaces. In fact, the RHCP component of the scattered signal is identically zero at incidence angles below the Brewster angle for a perfectly smooth planar surface. Newer versions of GNSS-R sensors are being built with dual-polarization capability, in which the GNSS-R antenna receives both LHCP and RHCP signals, and parallel receiver channels generate DDM measurements at both polarizations. For coherent reflections from land surfaces, the relationship between the transmitted GNSS signal and received GNSS-R signals is a generalization of the single polarization expressions given above by (2)–(7). In the dual-polarization case, the received power can be expressed as [103]

$$\begin{bmatrix} P_L^g \\ P_R^g \end{bmatrix} = \frac{\lambda^2 P^T}{(4\pi)^2 \left(R^T + R^R\right)^2} \begin{bmatrix} G_{LL}^R & G_{LR}^R \\ G_{RL}^R & G_{RR}^R \end{bmatrix} \begin{bmatrix} \Gamma_{LR} & \Gamma_{LL} \\ \Gamma_{RR} & \Gamma_{RL} \end{bmatrix} \begin{bmatrix} G_R^T \\ G_L^T \end{bmatrix} e^{-(2kh\cos\theta + 2\tau\sec\theta)^2} \quad (8)$$

where P_p^g is the power received by the p-pol channel ($p = L$ for LHCP and $p = R$ for RHCP), G_{pq}^R is the receive antenna gain for a q-pol incident signal received by the p-pol channel, Γ_{pq} is the surface reflectivity for a q-pol incident and p-pol scattered signal, and G_p^T is the transmit antenna gain for the p-pol transmitted signal. In practice, GNSS transmit signals are often assumed to be purely RHCP, in which case $G_L^T = 0$. The other terms in (8) are defined similarly as in (2) and (7), and it is understood

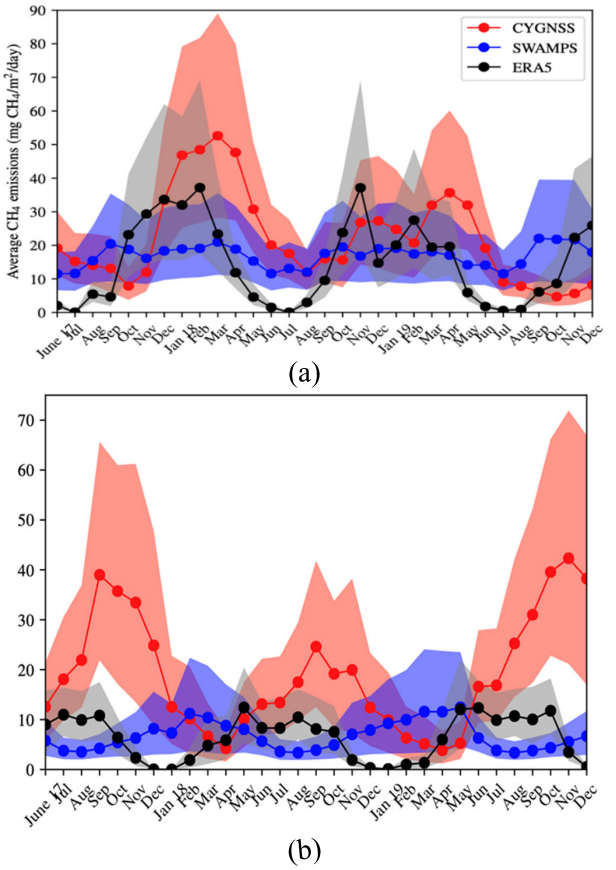


Fig. 12. *(a) Modeled monthly methane emission over the Pantanal using: red: CYGNSS-based maps, blue: SWAMPS product, and black: ERA5 rainfall-driven estimate. (b) Same but over the Sudd wetland in South Sudan.*

that the scattered signal is located at the point of specular reflection.

The first spaceborne dual-polarization GNSS-R measurements were made by repurposing the software-defined radar receiver on the NASA SMAP satellite [104], [105]. More recent airborne GNSS-R measurements have also been reported [106]. These measurements are still quite new, and determining their potential remote sensing value is an active area of research. They hold the promise of reducing the sensitivity of soil moisture retrievals to variations in surface roughness and vegetation. This can be seen by noting that the surface reflectivity Γ in (8) is polarization-dependent, whereas the surface roughness h and vegetation optical depth τ are not. It may be possible to reduce the effects of the exponential term in (8) by evaluating the ratio between the *L*- and *R*-polarized received signals. However, initial results examining this behavior for GNSS-R reflections from sea ice indicate that the effects of roughness do not fully cancel [120]. How well the approach works over land for soil moisture retrievals remains to be seen.

B. Higher Receive Antenna Gain

The receive antenna used on the CYGNSS satellites is a 2×3 element planar phased array with a peak gain of $\sim$14 dBi [107]. Other spaceborne GNSS-R sensors have used 1×3, 2×2, and 2×3 element planar phased arrays with peak gains of $\sim$11–14 dBi. The receive antenna gain scales the signal strength entering the receiver and so has a direct impact on the SNR of the measurement. The uncertainty of some science data products derived from GNSS-R measurements is driven by SNR and others are not. An example of the latter is water inundation mapping, for which the signal reflected from smooth water is very strong and the mapping uncertainty is primarily dependent on the variability of reflections from land clutter near the water bodies, not on the SNR of the received signal. An example of the former is wind speed determination in hurricanes. In this case, storm-level wind speeds are associated with extremely rough seas and very low received GNSS signal power. The weak SNR of GNSS reflections in hurricanes is the primary cause of the uncertainty in the corresponding wind speed retrievals. This correspondence is analyzed in detail in [108], and it is estimated that a peak antenna gain of $\sim$19 dBi is required in order to reliably be able to distinguish between a Cat 4 hurricane and a Cat 5 hurricane. This will require a planar phased array antenna with approximately 4×5 elements.

C. Real-Time DDM Processing Improvements

A number of DDM processing options have come to light over the course of CYGNSS operations that would greatly enhance the science returns of future missions. The main CYGNSS product consists of four parallel single polarization (LHCP) power DDMs of size 11 Doppler bins $\times$ 17 delay bins. Occasionally, CYGNSS can download the Full Level 0 DDM of 20 Doppler and 128 delay bins, which provides a greater surface extent observation of the reflected power, as well as roughly 1-min captures of the raw intermediate frequency (raw-IF) data, which allows comprehensive on-ground postprocessing over short intervals. The existence of the CYGNSS raw IF data has demonstrated the utility of having access to the reflected signal phase information, notably in cases of coherent surface reflections. Additionally, with the exponential increase in transmitters of opportunity as new GNSS constellations come online, an increasing number of parallel surface reflections are available to improve spatial coverage that the next generation of instruments should utilize.

For the case of reflected signal phase information in the coherent reflection cases, the use of CYGNSS raw-IF data has shown that precise relative surface altimetry observations can be performed from the ocean and inland rivers [84], [85]. These applications require that the processing retains the in-phase and quadrature signal components to allow tracking of the signal carrier phase over the reflecting surface. The conditions where this is possible occur over only a small fraction of the Earth surface, but the science payoff is potentially very large if future instruments have the ability to "target" known regions of coherent reflection and retain the phase information contained in reflection tracks across these areas.

Most fully operational GNSS constellations contain roughly a few dozen satellites (i.e., the number of GPS transmitters is often slightly larger than its requirement at about 30). Other GNSS constellations such as Galileo, GLONASS, and BeiDou (to name only the main global ones) are also expected to be of comparable constellation size. This will increase the number of bistatic transmitters of opportunity from roughly 30 using GPS alone to well over 100 using all in-view GNSS transmitters. This places additional requirements on the next generation of receivers to be able to process multiple signals from all of these GNSS constellations (with different frequencies and modulation schemes) as well as having the increased processing capacity to track all viable GNSS-R measurements in parallel, and generate Level 0 DDMs for all reflections falling within the main beams of the observatory's downward looking science antennas.

In summary, it is expected that new GNSS-R instruments will: 1) contain additional input channels for processing reflections in two parallel polarizations; 2) carry higher gain antennas for improved sensitivity in low SNR environments; 3) be capable of processing and retaining reflected signal phase information over regions where coherent reflections are common; and 4) be capable of targeting and tracking surface reflections from multiple GNSS constellations and generating an increased number of parallel observations, which will significantly increase the overall surface coverage of future GNSS-R missions and constellations.

VII. CONCLUSION

The idea of using GPS signals to create a "multistatic scatterometer" was first proposed in 1988 but was considered unworkable because the power density of the scattered signal would be too low to reliably detect [1]. That assessment drastically underestimated the magnitude of the bistatic radar cross section of the Earth surface for a specular forward scattering geometry. Ten years later, in 1998, the practical viability of GNSS-R was empirically demonstrated by an airborne GNSS navigation receiver that had been modified to measure GPS signals reflected from the surface of the ocean [3]. Multiple spaceborne technology demonstration missions soon followed, in 2002 [10], 2005 [12], and 2014 [22]. In parallel with these developments of GNSS-R receiver technology and signal processing algorithms, the theoretical description of bistatic scattering from the ocean surface was adapted to the specific case of GNSS signals and signal processing [4], [5], [8]. This early work established the empirical and theoretical foundation for everything that followed.

The first spaceborne GNSS-R mission designed not to demonstrate technology but to achieve specific scientific objectives was the NASA CYGNSS, which launched in December 2016 and is still operating. CYGNSS was designed to measure surface winds in tropical cyclones with the spatial and temporal sampling required to resolve their rapid intensification phase. In order to meet the spatial sampling requirement, the mission needed a constellation of six satellites (eight were flown to provide adequate system-level redundancy). To meet the temporal sampling requirement, the satellites needed to operate continuously, with a ∼100% GNSS-R observing duty cycle, and the downlink communication system needed to be able to get all of the DDM data to the ground. These three aspects of the mission architecture (eight satellites, 24/7 operation, and 100% data downlink) have led to the creation of a dense archival record of global DDM observations spanning more than eight years. This treasure trove of data, plus the fact that it is freely available on public-facing NASA file servers [109], has helped support and grow a new research community of GNSS-R retrieval algorithm developers and data product applications specialists.

The original application envisioned for GNSS-R measurements from space was SSH altimetry [2]. The first demonstrated capabilities were altimetry [115] and ocean surface winds [6], [7], [12]. Another early focus was on soil moisture retrievals [16], [17]. While these are the most mature uses for GNSS-R measurements, as the CYGNSS data archive grows, additional geophysical retrievals and scientific applications continue to be discovered and refined. These include (just to name a few) the forecasting of precipitation structure in hurricanes [89], the tracking of disappearing permafrost [87], the modeling of methane emission from wetland inundation [102], and the seasonal dependence of ocean microplastics in the Great Pacific Garbage Patch [99]. One significant limitation of the CYGNSS data archive should also be noted, which results from the mission's focus on tropical cyclones. Because its satellites orbit with a 35° inclination, the latitudinal coverage is restricted to ∼39°N–39°S. This limits its value for cryospheric science investigations. Luckily, other missions, including the early UK-DMC and TDS satellites as well as other more recent follow-on missions, are in polar orbits. The early ice detection work done with UK-DMC [14] has since grown to include the determination of ice height using TDS [110] and Spire [111] data, and ice thickness using observations by FY-3E [112]. These are just a few of the many applications that are possible, and the GNSS-R research community is still young and growing. New and improved algorithms to estimate geophysical parameters and new applications that make use of them can be expected to appear in the future. ■

REFERENCES

[1] C. D. Hall and R. A. Cordey, "Multistatic scatterometry," in *Proc. Int. Geosci. Remote Sens. Symp., 'Remote Sens., Moving Toward 21st Century'*, May 1988, pp. 13–16.

[2] M. Martín-Neira, "A passive reflectometry and interferometry system (PARIS): Application to ocean altimetry," *ESA J.*, vol. 17, no. 4, pp. 331–355, Dec. 1993.

[3] J. L. Garrison, S. J. Katzberg, and M. I. Hill, "Effect of sea roughness on bistatically scattered range coded signals from the global positioning system," *Geophys. Res. Lett.*, vol. 25, no. 13, pp. 2257–2260, Jul. 1998.

[4] A. Komjathy, V. U. Zavorotny, P. Axelrad, G. H. Born, and J. L. Garrison, "GPS signal scattering from sea surface: Wind speed retrieval using experimental data and theoretical model," *Remote Sens. Environ.*, vol. 73, no. 1, pp. 162–174, 2000.

[5] M. Armatys, "Estimation of sea surface winds using reflected GPS signals," Ph.D. dissertation, Dept. Aerospace Eng. Sci., Univ. Colorado, Boulder, CO, USA, 2001.

[6] J. L. Garrison, A. Komjathy, V. U. Zavorotny, and S. J. Katzberg, "Wind speed measurement using forward scattered GPS signals," *IEEE Trans. Geosci. Remote Sens.*, vol. 40, no. 1, pp. 50–65, Jan. 2002.

[7] E. Cardellach, G. Ruffini, D. Pino, A. Rius, A. Komjathy, and J. Garrison, "Mediterranean balloon experiment: Ocean wind speed sensing from the stratosphere using GPS reflections," *Remote Sens. Environ.*, vol. 88, pp. 351–362, Apr. 2003.

[8] V. U. Zavorotny and A. G. Voronovich, "Scattering of GPS signals from the ocean with wind remote sensing application," *IEEE Trans. Geosci. Remote Sens.*, vol. 38, no. 2, pp. 951–964, Mar. 2000.

[9] T. Elfouhaily, B. Chapron, K. Katsaros, and D. Vandemark, "A unified directional spectrum for long and short wind-driven waves," *J. Geophys. Res., Oceans*, vol. 102, no. C7, pp. 15781–15796, Jul. 1997.

[10] S. T. Lowe, J. L. La Brecque, C. Zuffada, L. J. Romans, L. E. Young, and G. A. Hajj, "First spaceborne observation of an Earth-reflected GPS signal," *Radio Sci.*, vol. 37, no. 1, pp. 1–28, Jan. 2002.

[11] M. J. Unwin, S. Gleason, and M. Brennan, "The space GPS reflectometry experiment on the U.K. disaster monitoring constellation satellite," in *Proc. ION-GPS/GNSS*, Sep. 2003, pp. 2656–2663.

[12] S. Gleason et al., "Detection and processing of bistatically reflected GPS signals from low earth orbit for the purpose of ocean remote sensing," *IEEE Trans. Geosci. Remote Sens.*, vol. 43, no. 6, pp. 1229–1241, Jun. 2005, doi: 10.1109/TGRS.2005.845643.

[13] S. Gleason, "Remote sensing of ocean, ice and land surfaces using bistatically scattered GNSS signals from low Earth orbit," Ph.D. dissertation, Dept. Eng. Physical Sci., Univ. Surrey, Guildford, U.K., 2006.

[14] S. Gleason, "Towards sea ice remote sensing with space detected GPS signals: Demonstration of technical feasibility and initial consistency check using low resolution sea ice information," *Remote Sens.*, vol. 2, no. 8, pp. 2017–2039, Aug. 2010.

[15] S. Gleason, "Space-based GNSS scatterometry: Ocean wind sensing using an empirically calibrated model," *IEEE Trans. Geosci. Remote Sens.*, vol. 51, no. 9, pp. 4853–4863, Sep. 2013.

[16] D. Masters, P. Axelrad, and S. Katzberg, "Initial results of land-reflected GPS bistatic radar measurements in SMEX02," *Remote Sens. Environ.*, vol. 92, no. 4, pp. 507–520, Sep. 2004.

[17] D. Masters, "Surface remote sensing applications of GNSS bistatic radar: Soil moisture and aircraft

altimetry," Ph.D. dissertation, Dept. Aerospace Eng. Sci., Univ. Colorado, Boulder, CO, USA, 2004.
[18] M. B. Rivas, J. A. Maslanik, and P. Axelrad, "Bistatic scattering of GPS signals off Arctic sea ice," *IEEE Trans. Geosci. Remote Sens.*, vol. 48, no. 3, pp. 1548–1553, Mar. 2010.
[19] C. S. Ruf et al., "New ocean winds satellite mission to probe hurricanes and tropical convection," *Bull. Amer. Meteorological Soc.*, vol. 97, no. 3, pp. 385–395, Mar. 2016, doi: 10.1175/bams-d-14-00218.1.
[20] P. Jales, "Spaceborne receiver design for scatterometric GNSS reflectometry," Ph.D. thesis, Dept. Eng. Physical Sci., Univ. Surrey, Guildford, U.K., 2012.
[21] M. Unwin et al., "Remote sensing using GPS signals—The SGR-ReSI instrument," in *Proc. 25th Annu. AIAA/USU Conf. Small Satell.*, Logan, UT, USA, 2011, pp. 1–8.
[22] M. Unwin, S. Duncan, P. Jales, P. Blunt, and M. Brenchley, "Implementing GNSS reflectometry in space on the TechDemoSat-1 mission," in *Proc. Inst. Navigat.*, Sep. 2014, pp. 1222–1235.
[23] G. Foti et al., "Spaceborne GNSS reflectometry for ocean winds: First results from the U.K. TechDemoSat-1 mission," *Geophys. Res. Lett.*, vol. 42, no. 13, pp. 5435–5441, Jul. 2015, doi: 10.1002/2015gl064204.
[24] C. Chew, R. Shah, C. Zuffada, G. Hajj, D. Masters, and A. J. Mannucci, "Demonstrating soil moisture remote sensing with observations from the U.K. TechDemoSat-1 satellite mission," *Geophys. Res. Lett.*, vol. 43, no. 7, pp. 3317–3324, Apr. 25, 2016, doi: 10.1002/2016gl068189.
[25] S. Gleason, S. Lowe, and V. Zavorotny, "GNSS applications and methods," in *Remote Sensing With Bistatic GNSS Reflections*. Norwood, MA, USA: Artech House, 2009, pp. 399–436.
[26] V. U. Zavorotny, S. Gleason, E. Cardellach, and A. Camps, "Tutorial on remote sensing using GNSS bistatic radar of opportunity," *IEEE Geosci. Remote Sens. Mag.*, vol. 2, no. 4, pp. 8–45, Dec. 2014, doi: 10.1109/MGRS.2014.2374220.
[27] (2015). *CYGNSS Sampling Tutorial Video*. [Online]. Available: https://youtu.be/sbQ0m5lxLD8
[28] C. D. Bussy-Virat, C. S. Ruf, and A. J. Ridley, "Relationship between temporal and spatial resolution for a constellation of GNSS-R satellites," *IEEE J. Sel. Topics Appl. Earth Observ. Remote Sens.*, vol. 12, no. 1, pp. 16–25, Jan. 2019, doi: 10.1109/JSTARS.2018.2833426.
[29] C. Ruf et al., "In-orbit performance of the constellation of CYGNSS hurricane satellites," *Bull. Amer. Meteorological Soc.*, vol. 100, no. 10, pp. 2009–2023, Oct. 2019, doi: 10.1175/bams-d-18-0337.1.
[30] C. S. Ruf et al., "A new paradigm in Earth environmental monitoring with the CYGNSS small satellite constellation," *Sci. Rep.*, vol. 8, no. 1, p. 8782, Jun. 2018, doi: 10.1038/s41598-018-27127-4.
[31] (2025). *CYGNSS Mission Science Data Products*. [Online]. Available: https://cygnss.engin.umich.edu/data-products/
[32] C. Jing et al., "GNSS-R from the Bufeng-1 twin satellites for sea surface winds under hurricane condition," in *Proc. IEEE Int. Geosci. Remote Sens. Symp. IGARSS*, Jul. 2021, pp. 1299–1302, doi: 10.1109/IGARSS47720.2021.9554797.
[33] C. Jing et al., "A review of the BuFeng-1 GNSS-R mission: Calibration and validation results of sea surface and land surface," *Geo-Spatial Inf. Sci.*, vol. 27, no. 3, pp. 638–652, May 2024, doi: 10.1080/10095020.2024.2330547.
[34] G. Yang et al., "FY3E GNOS II GNSS reflectometry: Mission review and first results," *Remote Sens.*, vol. 14, no. 4, p. 988, Feb. 2022, doi: 10.3390/rs14040988.
[35] F. Huang et al., "Progress on the GNSS-R product from Fengyun-3 missions," in *Proc. IEEE Int. Geosci. Remote Sens. Symp.*, Athens, Greece, Jul. 2024, pp. 6717–6720, doi: 10.1109/IGARSS53475.2024.10640688.
[36] J.-C. Juang, Y.-F. Tsai, and C.-T. Lin, "TRITON GNSS-R mission: Preliminary results and perspectives," in *Proc. IEEE Int. Geosci. Remote Sens. Symp.*, Athens, Greece, Jul. 2024, pp. 6725–6728, doi: 10.1109/IGARSS53475.2024.10642499.
[37] M. J. Unwin et al., "An introduction to the HydroGNSS GNSS reflectometry remote sensing mission," *IEEE J. Sel. Topics Appl. Earth Observ. Remote Sens.*, vol. 14, pp. 6987–6999, 2021, doi: 10.1109/JSTARS.2021.3089550.
[38] P. Jales et al., "Spire global's operational GNSS-reflectometry constellation for Earth surface observations," in *Proc. IEEE Int. Geosci. Remote Sens. Symp.*, Pasadena, CA, USA, Jul. 2023, pp. 884–887, doi: 10.1109/IGARSS52108.2023.10282940.
[39] X. Liu et al., "Performance validation of sea surface wind speed retrieval algorithms and products from the Chinese Tianmu-1 constellation GNSS-R: First results on comparison with other wind speed products," *IEEE J. Sel. Topics Appl. Earth Observ. Remote Sens.*, vol. 18, pp. 5189–5203, 2025, doi: 10.1109/JSTARS.2025.3527026.
[40] C. Ruf, R. Miller, T. Butler, and C. C. Chen, "Next generation global navigation satellite system reflectometry receiver (NGRx)," U.S. Patent 18 129 226, Mar. 31, 2023.
[41] D. Masters et al., "New polarimetric GNSS-R observations of the water cycle from the muon space MuSat-2 SmallSat mission," in *Proc. 105th Annu. Meeting Amer. Meteorological Soc.*, 2025. [Online]. Available: https://doi.org/10.48550/arXiv.2412.00072
[42] P. Misra and P. Enge, *Global Positioning System: Signals, Measurements, and Performance*, 2nd ed., Lincoln, MA, USA: Ganga-Jamuna, 2011.
[43] Y. J. Morton et al., *Position, Navigation, and Timing Technologies in the 21st Century: Integrated Satellite Navigation, Sensor Systems, and Civil Applications, Volume 1*. Hoboken, NJ, USA: Wiley, 2020.
[44] E. D. Kaplan and C. Hegarty, *Understanding GPS: Principles and Applications*, 2nd ed., Norwood, MA, USA: Artech House, 2005.
[45] S. Gleason and D. Gebre-Egziabher, *GNSS Applications and Methods*. Norwood, MA, USA: Artech House, 2009.
[46] P. Groves, *Principles of GNSS, Inertial, and Multisensor Integrated Navigation Systems*. Norwood, MA, USA: Artech House, 2008, pp. 399–436.
[47] P. Beckmann and A. Spizzichino, *The Scattering of Electromagnetic Waves From Rough Surfaces*. Norwood, MA, USA: Artech House, 1987.
[48] NASA. (Dec. 8, 2023). *Level 1B DDM Calibration Algorithm Theoretical Basis Document. Rev 6 (v3.2)*. [Online]. Available: https://archive.podaac.earthdata.nasa.gov/podaac-ops-cumulus-docs/cygnss/open/L1/docs/148-0137_L1B_DDM_Calibration_ATBD_R6.pdf
[49] S. Gleason, A. O'Brien, A. Russel, M. M. Al-Khaldi, and J. T. Johnson, "Geolocation, calibration and surface resolution of CYGNSS GNSS-R land observations," *Remote Sens.*, vol. 12, no. 8, p. 1317, Apr. 2020, doi: 10.3390/rs12081317.
[50] M. M. Al-Khaldi, J. T. Johnson, S. Gleason, E. Loria, A. J. O'Brien, and Y. Yi, "An algorithm for detecting coherence in cyclone global navigation satellite system mission Level-1 delay-Doppler maps," *IEEE Trans. Geosci. Remote Sens.*, vol. 59, no. 5, pp. 4454–4463, May 2021.
[51] H. Carreno-Luengo, C. S. Ruf, S. Gleason, and A. Russel, "A new multiresolution CYGNSS data product for fully and partially coherent scattering," *IEEE Trans. Geosci. Remote Sens.*, vol. 61, no. 4408118, 2023, doi: 10.1109/TGRS.2023.3318639.
[52] S. Gleason, "A real-time on-orbit signal tracking algorithm for GNSS surface observations," *Remote Sens.*, vol. 11, no. 16, p. 1858, Aug. 2019, doi: 10.3390/rs11161858.
[53] S. Gleason, H. C. Luengo, C. Ruf, and A. Russel, "Comparison of GNSS-R delay Doppler map processing algorithms," in *Proc. IEEE Int. Geosci. Remote Sens. Symp.*, Athens, Greece, Jul. 2024, pp. 6356–6359, doi: 10.1109/IGARSS53475.2024.10641548.
[54] NASA. (Dec. 8, 2023). *CYGNSS Level 1A DDM Calibration Algorithm Theoretical Basis Document. Rev 4 (v3.2)*. [Online]. Available: https://archive.podaac.earthdata.nasa.gov/podaac-ops-cumulus-docs/cygnss/open/L1/docs/148-0136_L1A_DDM_Calibration_ATBD_R4.pdf
[55] S. Gleason, C. S. Ruf, M. P. Clarizia, and A. J. O'Brien, "Calibration and unwrapping of the normalized scattering cross section for the cyclone global navigation satellite system," *IEEE Trans. Geosci. Remote Sens.*, vol. 54, no. 5, pp. 2495–2509, May 2016.
[56] M. P. Clarizia and C. S. Ruf, "On the spatial resolution of GNSS reflectometry," *IEEE Geosci. Remote Sens. Lett.*, vol. 13, no. 8, pp. 1064–1068, Aug. 2016, doi: 10.1109/LGRS.2016.2565380.
[57] A. G. Voronovich and V. U. Zavorotny, "Bistatic radar equation for signals of opportunity revisited," *IEEE Trans. Geosci. Remote Sens.*, vol. 56, no. 4, pp. 1959–1968, Apr. 2018, doi: 10.1109/TGRS.2017.2771253.
[58] A. M. Balakhder, M. M. Al-Khaldi, and J. T. Johnson, "On the coherency of ocean and land surface specular scattering for GNSS-R and signals of opportunity systems," *IEEE Trans. Geosci. Remote Sens.*, vol. 57, no. 12, pp. 10426–10436, Dec. 2019, doi: 10.1109/TGRS.2019.2935257.
[59] A. Camps, "Spatial resolution in GNSS-R under coherent scattering," *IEEE Geosci. Remote Sens. Lett.*, vol. 17, no. 1, pp. 32–36, Jan. 2020, doi: 10.1109/LGRS.2019.2916164.
[60] NASA. (Dec. 8, 2023). *CYGNSS Level 2 Wind Speed Retrieval Algorithm Theoretical Basis Document. Rev 8 (v3.2)*.[Online]. Available: https://archive.podaac.earthdata.nasa.gov/podaac-ops-cumulus-docs/cygnss/open/L2/docs/148-0138_L2_Wind_Speed_Retrieval_ATBD_R8.pdf
[61] M. P. Clarizia and C. S. Ruf, "Wind speed retrieval algorithm for the cyclone global navigation satellite system (CYGNSS) mission," *IEEE Trans. Geosci. Remote Sens.*, vol. 54, no. 8, pp. 4419–4432, Aug. 2016, doi: 10.1109/TGRS.2016.2541343.
[62] C. S. Ruf and R. Balasubramaniam, "Development of the CYGNSS geophysical model function for wind speed," *IEEE J. Sel. Topics Appl. Earth Observ. Remote Sens.*, vol. 12, no. 1, pp. 66–77, Jan. 2019, doi: 10.1109/JSTARS.2018.2833075.
[63] D. Pascual, M. P. Clarizia, and C. S. Ruf, "Improved CYGNSS wind speed retrieval using significant wave height correction," *Remote Sens.*, vol. 13, no. 21, p. 4313, Oct. 2021, doi: 10.3390/rs13214313.
[64] C. Ruf et al., "Characterization of CYGNSS ocean surface wind speed products," *Remote Sens.*, vol. 16, no. 22, p. 4341, Nov. 2024, doi: 10.3390/rs16224341.
[65] A. M. Warnock, C. S. Ruf, A. Russel, M. M. Al-Khaldi, and R. Balasubramaniam, "CYGNSS level 3 merged wind speed data product for storm force and surrounding environmental winds," *IEEE J. Sel. Topics Appl. Earth Observ. Remote Sens.*, vol. 17, pp. 6189–6200, 2024, doi: 10.1109/JSTARS.2024.3379934.
[66] M. P. Clarizia, C. Ruf, P. Cipollini, and C. Zuffada, "First spaceborne observation of sea surface height using GPS-reflectometry," *Geophys. Res. Lett.*, vol. 43, no. 2, pp. 767–774, Jan. 2016, doi: 10.1002/2015gl066624.
[67] J. Mashburn, P. Axelrad, C. Zuffada, E. Loria, A. O'Brien, and B. Haines, "Improved GNSS-R ocean surface altimetry with CYGNSS in the seas of Indonesia," *IEEE Trans. Geosci. Remote Sens.*, vol. 58, no. 9, pp. 6071–6087, Sep. 2020, doi: 10.1109/TGRS.2020.2973079.
[68] E. Cardellach et al., "First precise spaceborne sea surface altimetry with GNSS reflected signals," *IEEE J. Sel. Topics Appl. Earth Observ. Remote Sens.*, vol. 13, pp. 102–112, 2020, doi:

10.1109/JSTARS.2019.2952694.
[69] S. H. Yueh, R. Shah, M. J. Chaubell, A. Hayashi, X. Xu, and A. Colliander, "A semiempirical modeling of soil moisture, vegetation, and surface roughness impact on CYGNSS reflectometry data," *IEEE Trans. Geosci. Remote Sens.*, vol. 60, pp. 1–17, 2020, doi: 10.1109/TGRS.2020.3035989.
[70] C. C. Chew and E. E. Small, "Soil moisture sensing using spaceborne GNSS reflections: Comparison of CYGNSS reflectivity to SMAP soil moisture," *Geophys. Res. Lett.*, vol. 45, no. 9, pp. 4049–4057, May 2018, doi: 10.1029/2018GL077905.
[71] C. Chew and E. Small, "Description of the UCAR/CU soil moisture product," *Remote Sens.*, vol. 12, no. 10, p. 1558, May 2020.
[72] H. Kim and V. Lakshmi, "Use of cyclone global navigation satellite system (CyGNSS) observations for estimation of soil moisture," *Geophys. Res. Lett.*, vol. 45, no. 16, pp. 8272–8282, Aug. 2018, doi: 10.1029/2018gl078923.
[73] O. Eroglu, M. Kurum, D. Boyd, and A. C. Gurbuz, "High spatio-temporal resolution CYGNSS soil moisture estimates using artificial neural networks," *Remote Sens.*, vol. 11, no. 19, p. 2272, Sep. 2019, doi: 10.3390/rs11192272.
[74] P. Setti and S. Tabibi, "Comprehensive analysis of CYGNSS GNSS-R data for enhanced soil moisture retrieval," *IEEE J. Sel. Topics Appl. Earth Observ. Remote Sens.*, vol. 18, pp. 663–679, 2025.
[75] *Level 3 Soil Moisture Version 3.2*, CYGNSS, Pasadena, CA, USA, 2025, doi: 10.5067/CYGNU-L3S32.
[76] K. Jensen, K. McDonald, E. Podest, N. Rodriguez-Alvarez, V. Horna, and N. Steiner, "Assessing L-band GNSS-reflectometry and imaging radar for detecting sub-canopy inundation dynamics in a tropical wetlands complex," *Remote Sens.*, vol. 10, no. 9, p. 1431, Sep. 2018, doi: 10.3390/rs10091431.
[77] M. Morris, C. Chew, J. T. Reager, R. Shah, and C. Zuffada, "A novel approach to monitoring wetland dynamics using CYGNSS: Everglades case study," *Remote Sens. Environ.*, vol. 233, Nov. 2019, Art. no. 111417.
[78] C. Chew and E. Small, "Estimating inundation extent using CYGNSS data: A conceptual modeling study," *Remote Sens. Environ.*, vol. 246, Sep. 2020, Art. no. 111869.
[79] C. Gerlein-Safdi and C. S. Ruf, "A CYGNSS-based algorithm for the detection of inland waterbodies," *Geophys. Res. Lett.*, vol. 46, no. 21, pp. 12065–12072, Nov. 2019, doi: 10.1029/2019gl085134.
[80] T. Pu, C. Gerlein-Safdi, Y. Xiong, M. Li, E. A. Kort, and A. A. Bloom, "Berkeley-RWAWC: A new CYGNSS-based watermask unveils unique observations of seasonal dynamics in the tropics," *Water Resources Res.*, vol. 60, no. 7, Jul. 2024, doi: 10.1029/2024wr037060.
[81] *UC Berkeley CYGNSS Level 3 RWAWC Watermask Version 3.1*, CYGNSS, Pasadena, CA, USA, 2025, doi: 10.5067/CYGNS-L3W31.
[82] A. Warnock, C. S. Ruf, and A. L. Knoll, "Characterization of river width measurement capability by space borne GNSS-reflectometry," *Remote Sens.*, vol. 16, no. 8, p. 1446, Apr. 2024, doi: 10.3390/rs16081446.
[83] A. Warnock and C. Ruf, "Response to variations in river flowrate by a spaceborne GNSS-R river width estimator," *Remote Sens.*, vol. 11, no. 20, p. 2450, Oct. 2019, doi: 10.3390/rs11202450.
[84] Y. Wang and Y. J. Morton, "River slope observation from spaceborne GNSS-R carrier phase measurements: A case study," *IEEE Geosci. Remote Sens. Lett.*, vol. 19, pp. 1–5, 2022, doi: 10.1109/LGRS.2021.3127750.
[85] Y. Wang et al., "Measuring river slope using spaceborne GNSS reflectometry: Methodology and first performance assessment," *Remote Sens. Environ.*, vol. 318, Mar. 2025, Art. no. 114597, doi: 10.1016/j.rse.2025.114597.
[86] H. Carreno-Luengo and C. S. Ruf, "Retrieving freeze/thaw surface state from CYGNSS measurements," *IEEE Trans. Geosci. Remote Sens.*, vol. 60, no. 4302313, 2022, doi: 10.1109/TGRS.2021.3120932.
[87] H. Carreno-Luengo and C. S. Ruf, "Mapping freezing and thawing surface state periods with the CYGNSS based F/T seasonal threshold algorithm," *IEEE J. Sel. Topics Appl. Earth Observ. Remote Sens.*, vol. 15, pp. 9943–9952, 2022, doi: 10.1109/JSTARS.2022.3216463.
[88] Z. Cui, Z. Pu, V. Tallapragada, R. Atlas, and C. S. Ruf, "A preliminary impact study of CYGNSS ocean surface wind speeds on numerical simulations of hurricanes," *Geophys. Res. Lett.*, vol. 46, no. 5, pp. 2984–2992, Mar. 2019, doi: 10.1029/2019gl082236.
[89] Z. Pu, Y. Wang, X. Li, C. Ruf, L. Bi, and A. Mehra, "Impacts of assimilating CYGNSS satellite ocean-surface wind on prediction of landfalling hurricanes with the HWRF model," *Remote Sens.*, vol. 14, no. 9, p. 2118, Apr. 2022, doi: 10.3390/rs14092118.
[90] B. McNoldy, B. Annane, S. Majumdar, J. Delgado, L. Bucci, and R. Atlas, "Impact of assimilating CYGNSS data on tropical cyclone analyses and forecasts in a regional OSSE framework," *Mar. Technol. Soc. J.*, vol. 51, no. 1, pp. 7–15, Jan. 2017, doi: 10.4031/mtsj.51.1.1.
[91] J. Crespo, D. Posselt, and S. Asharaf, "CYGNSS surface heat flux product development," *Remote Sens.*, vol. 11, no. 19, p. 2294, Oct. 2019, doi: 10.3390/rs11192294.
[92] J. A. Crespo, D. J. Posselt, C. M. Naud, and C. Bussy-Virat, "Assessing CYGNSS's potential to observe extratropical fronts and cyclones," *J. Appl. Meteorol. Climatol.*, vol. 56, no. 7, pp. 2027–2034, Jul. 2017, doi: 10.1175/jamc-d-17-0050.1.
[93] J. A. Crespo, C. M. Naud, and D. J. Posselt, "CYGNSS observations and analysis of low-latitude extratropical cyclones," *J. Appl. Meteorol. Climatol.*, vol. 60, no. 4, pp. 527–541, Apr. 2021, doi: 10.1175/jamc-d-20-0190.1.
[94] C. M. Naud, J. A. Crespo, and D. J. Posselt, "On the relationship between CYGNSS surface heat fluxes and the lifecycle of low-latitude ocean extratropical cyclones," *J. Appl. Meteorol. Climatol.*, vol. 60, no. 11, pp. 1575–1590, Oct. 2021, doi: 10.1175/jamc-d-21-0074.1.
[95] M. B. Natoli and E. D. Maloney, "Intraseasonal variability of the diurnal cycle of precipitation in the Philippines," *J. Atmos. Sci.*, vol. 76, no. 11, pp. 3633–3654, Nov. 2019.
[96] H. X. Bui, E. D. Maloney, E. M. Riley Dellaripa, and B. Singh, "Wind speed, surface flux, and intraseasonal convection coupling from CYGNSS data," *Geophys. Res. Lett.*, vol. 47, no. 21, Nov. 2020, Art. no. e2020GL090376, doi: 10.1029/2020gl090376.
[97] M. B. Natoli and E. D. Maloney, "Quasi-biweekly extensions of the monsoon winds and the Philippines diurnal cycle," *Monthly Weather Rev.*, vol. 149, no. 12, pp. 3939–3960, Dec. 2021.
[98] H. X. Bui, E. D. Maloney, E. Short, and E. M. Riley Dellaripa, "Diurnal cycle of wind speed and precipitation over the northern Australia coastal region: CYGNSS observations," *Geophys. Res. Lett.*, vol. 50, no. 8, pp. 1–12, Apr. 2023, doi: 10.1029/2023gl103005.
[99] M. C. Evans and C. S. Ruf, "Toward the detection and imaging of ocean microplastics with a spaceborne radar," *IEEE Trans. Geosci. Remote Sens.*, vol. 60, no. 4202709, 2022, doi: 10.1109/TGRS.2021.3081691.
[100] A. A. Bloom et al., "A global wetland methane emissions and uncertainty dataset for atmospheric chemical transport models (WetCHARTs version 1.0)," *Geosci. Model Develop.*, vol. 10, no. 6, pp. 2141–2156, Jun. 2017, doi: 10.5194/gmd-10-2141-2017.
[101] A. L. Ganesan et al., "Advancing scientific understanding of the global methane budget in support of the Paris agreement," *Global Biogeochemical Cycles*, vol. 33, no. 12, pp. 1475–1512, Dec. 2019, doi: 10.1029/2018gb006065.
[102] C. Gerlein-Safdi, A. A. Bloom, G. Plant, E. A. Kort, and C. S. Ruf, "Improving representation of tropical wetland methane emissions with CYGNSS inundation maps," *Global Biogeochemical Cycles*, vol. 35, no. 12, pp. 1–14, Dec. 2021, doi: 10.1029/2020gb006890.
[103] D. Bai, C. Ruf, A. O'Brien, and D. Moller, "Calibration of the airborne polarimetric GNSS-R sensor for the rongowai project," in *Proc. IEEE Int. Geosci. Remote Sens. Symp.*, Jul. 2024, pp. 725–728, doi: 10.1109/IGARSS53475.2024.10640409.
[104] N. Rodriguez-Alvarez, S. Misra, E. Podest, M. Morris, and X. Bosch-Lluis, "The use of SMAP-reflectometry in science applications: Calibration and capabilities," *Remote Sens.*, vol. 11, no. 20, p. 2442, Oct. 2019, doi: 10.3390/rs11202442.
[105] N. Rodriguez-Alvarez, J. F. Munoz-Martin, X. Bosch-Lluis, K. Oudrhiri, D. Entekhabi, and A. Colliander, "The first polarimetric GNSS-reflectometer instrument in space improves the SMAP mission's sensitivity over densely vegetated areas," *Sci. Rep.*, vol. 13, no. 1, p. 3722, Mar. 2023, doi: 10.1038/s41598-023-30805-7.
[106] D. Bai, C. S. Ruf, and D. Moller, "Calibration of the polarimetric GNSS-R sensor in the Rongowai mission," *IEEE Trans. Geosci. Remote Sens.*, vol. 63, no. 5801618, 2025, doi: 10.1109/TGRS.2025.3558131.
[107] C. Ruf et al., *CYGNSS Handbook*, 2nd ed., Ann Arbor, MI, USA: Univ. of Michigan Press, 2022, doi: 10.3998/mpub.12741920.
[108] R. Balasubramaniam and C. S. Ruf, "Development and application of a GNSS-R error model for hurricane winds," *IEEE J. Sel. Topics Appl. Earth Observ. Remote Sens.*, vol. 17, pp. 2336–2346, 2024, doi: 10.1109/JSTARS.2023.3344371.
[109] Univ. Michigan. (2025). *CYGNSS Mission Website*. [Online]. Available: https://cygnss.engin.umich.edu/data-products
[110] J. Cartwright, C. J. Banks, and M. Srokosz, "Improved GNSS-R bi-static altimetry and independent digital elevation models of Greenland and Antarctica from TechDemoSat-1," *Cryosphere*, vol. 14, no. 6, pp. 1909–1917, Jun. 2020, doi: 10.5194/tc-14-1909-2020.
[111] R. N. Buendía, S. Tabibi, M. Talpe, and I. Otosaka, "Ice sheet height retrievals from spire grazing angle GNSS-R," *Remote Sens. Environ.*, vol. 297, Nov. 2023, Art. no. 113757, doi: 10.1016/j.rse.2023.113757.
[112] Y. Xie and Q. Yan, "Retrieval of sea ice thickness using FY-3E/GNOS-II data," *Satell. Navigat.*, vol. 5, p. 17, Dec. 2024, doi: 10.1186/s43020-024-00138-5.
[113] G. Beyerle and K. Hocke, "Observation and simulation of direct and reflected GPS signals in radio occultation experiments," *Geophys. Res. Lett.*, vol. 28, no. 9, pp. 1895–1898, May 2001.
[114] G. Beyerle, K. Hocke, J. Wickert, T. Schmidt, C. Marquardt, and C. Reigber, "GPS radio occultations with CHAMP: A radio holographic analysis of GPS signal propagation in the troposphere and surface reflections," *J. Geophys. Res., Atmos.*, vol. 107, no. D24, pp. 4802–4815, Dec. 2002, doi: 10.1029/2001jd001402.
[115] E. Cardellach, C. O. Ao, M. De La Torre Juárez, and G. A. Hajj, "Carrier phase delay altimetry with GPS-reflection/occultation interferometry from low Earth orbiters," *Geophys. Res. Lett.*, vol. 31, no. 10, May 2004, Art. no. L10402, doi: 10.1029/2004gl019775.
[116] K. M. Larson, E. E. Small, E. D. Gutmann, A. L. Bilich, J. J. Braun, and V. U. Zavorotny, "Use of GPS receivers as a soil moisture network for water cycle studies," *Geophys. Res. Lett.*, vol. 35, no. 24, Dec. 2008, Art. no. L24405.
[117] E. D. Gutmann, K. M. Larson, M. W. Williams, F. G. Nievinski, and V. Zavorotny, "Snow measurement by GPS interferometric

reflectometry: An evaluation at Niwot Ridge, Colorado," *Hydrological Processes*, vol. 26, no. 19, pp. 2951–2961, Sep. 2012.

[118] K. M. Larson, "Unanticipated uses of the global positioning system," *Annu. Rev. Earth Planet. Sci.*, vol. 47, no. 1, pp. 19–40, May 2019, doi: 10.1146/annurev-earth-053018-060203.

[119] A. Dielacher, H. Fragner, and O. Koudelka, "PRETTY—Passive GNSS-reflectometry for CubeSats PRETTY—Passive GNSS-reflektometrie für CubeSats," *e i Elektrotechnik und Informationstechnik*, vol. 139, no. 1, pp. 25–32, Feb. 2022, doi: 10.1007/s00502-022-00993-7.

[120] A. M. Semmling et al., "Sea-ice concentration derived from GNSS reflection measurements in Fram strait," *IEEE Trans. Geosci. Remote Sens.*, vol. 57, no. 12, pp. 10350–10361, Dec. 2019, doi: 10.1109/TGRS.2019.2933911.

[121] R. Schroeder et al., "Development and evaluation of a multi-year fractional surface water data set derived from active/passive microwave remote sensing data," *Remote Sens.*, vol. 7, no. 12, pp. 16688–16732, Dec. 2015, doi: 10.3390/rs71215843.

[122] H. Hersbach et al., "The ERA5 global reanalysis," *Quart. J. Roy. Meteorological Soc.*, vol. 146, no. 730, pp. 1999–2049, Jul. 2020, doi: 10.1002/qj.3803.

ABOUT THE AUTHORS



Christopher Ruf (Life Fellow, IEEE) received the B.A. degree in physics from the Reed College, Portland, OR, USA, in 1982, and the Ph.D. degree in electrical and computer engineering from the University of Massachusetts at Amherst, Amherst, MA, USA, in 1987.

He is the Frederick Bartman Collegiate Professor of climate and space science and the Director of the Space Institute, University of Michigan, Ann Arbor, MI, USA, and also a Principal Investigator of the NASA Cyclone Global Navigation Satellite System Earth Venture Mission. His research interests include remote sensing methods, applications, and technology.

Prof. Ruf is a fellow of American Meteorological Society, the Vice Chair of Commission F of the U.S. National Committee for the Union Radio Scientifique Internationale, and a member of American Geophysical Union. He is the former Editor-in-Chief of IEEE TRANSACTIONS ON GEOSCIENCE AND REMOTE SENSING and has served on the editorial boards of *Radio Science*, the *Journal of Atmospheric and Oceanic Technology*, and *Scientific Reports*.



Scott Gleason (Senior Member, IEEE) received the B.S. degree in electrical and computer engineering from the State University of New York at Buffalo, Buffalo, NY, USA, in 1991, the M.S. degree in engineering from Stanford University, Stanford, CA, USA, in 1999, and the Ph.D. degree in applied physics from the University of Surrey, Guildford, U.K., in 2007.

He has worked in the areas of astronautics, remote sensing, and Global Navigation Satellite System (GNSS) for more than 20 years, including the NASA Goddard Space Flight Center, Greenbelt, MD, USA, the GPS Laboratory, Stanford University, Surrey Satellite Technology Ltd., Guildford, Concordia University, Montreal, QC, Canada, the Southwest Research Institute, San Antonio, TX, USA, the University Corporation for Atmospheric Research, Boulder, CO, USA, and the National Oceanography Centre, Southampton, U.K. He is currently the President of Daaxa LLC, Boulder, specializing in GNSS instruments, calibration, and remote sensing applications. He is the Co-Investigator of the Science Team and an Instrument Scientist for the NASA Cyclone GNSS (CYGNSS) Mission.